AFRL-RQ-WP-TR-2013-0163

SCRAMJET RESEARCH WITH FLIGHT-LIKE INFLOW CONDITIONS

Mark A. Hagenmaier, John Boles, and Ryan T. Milligan

Propulsion Technology Branch
High Speed Systems Division

JULY 2013
Final Report

STINFO COPY

AIR FORCE RESEARCH LABORATORY
AEROSPACE SYSTEMS DIRECTORATE
WRIGHT-PATTERSON AIR FORCE BASE, OH 45433-7542
AIR FORCE MATERIEL COMMAND
UNITED STATES AIR FORCE

NOTICE AND SIGNATURE PAGE

REPORT DOCUMENTATION PAGE

The public reporting burden for this collection of information is estimated to average 1 hour per response, including the time for reviewing instructions, searching existing data sources, gathering and maintaining the data needed, and completing and reviewing the collection of information. Send comments regarding this burden estimate or any other aspect of this collection of information, including suggestions for reducing this burden, to Department of Defense, Washington Headquarters Services, Directorate for Information Operations and Reports (0704-0188), 1215 Jefferson Davis Highway, Suite 1204, Arlington, VA 22202-4302. Respondents should be aware that notwithstanding any other provision of law, no person shall be subject to any penalty for failing to comply with a collection of information if it does not display a currently valid OMB control number. **PLEASE DO NOT RETURN YOUR FORM TO THE ABOVE ADDRESS**.

1. REPORT DATE (DD-MM-YY)	2. REPORT TYPE	3. DATES COVERED (From - To)
July 2013	Final	01 May 2009 – 01 May 2013

4. TITLE AND SUBTITLE	
SCRAMJET RESEARCH WITH FLIGHT-LIKE INFLOW CONDITIONS	**5a. CONTRACT NUMBER** In-house
	5b. GRANT NUMBER
	5c. PROGRAM ELEMENT NUMBER 61102F

6. AUTHOR(S)	
Mark A. Hagenmaier, John Boles, and Ryan T. Milligan	**5d. PROJECT NUMBER** 2308
	5e. TASK NUMBER N/A
	5f. WORK UNIT NUMBER Q0E8

7. PERFORMING ORGANIZATION NAME(S) AND ADDRESS(ES)	8. PERFORMING ORGANIZATION REPORT NUMBER
Propulsion Technology Branch (AFRL/RQHP) High Speed Systems Division Air Force Research Laboratory, Aerospace Systems Directorate Wright-Patterson Air Force Base, OH 45433-7542 Air Force Materiel Command, United States Air Force	AFRL-RQ-WP-TR-2013-0163

9. SPONSORING/MONITORING AGENCY NAME(S) AND ADDRESS(ES)	10. SPONSORING/MONITORING AGENCY ACRONYM(S)
Air Force Research Laboratory Aerospace Systems Directorate Wright-Patterson Air Force Base, OH 45433-7542 Air Force Materiel Command United States Air Force	AFRL/RQHP
	11. SPONSORING/MONITORING AGENCY REPORT NUMBER(S) AFRL-RQ-WP-TR-2013-0163

12. DISTRIBUTION/AVAILABILITY STATEMENT
Approved for public release; distribution unlimited.

13. SUPPLEMENTARY NOTES
PA Case Number: 88ABW-2013-3689; Clearance Date: 19 Aug 2013. This report contains color.

14. ABSTRACT
Studies of flow distortion on fundamental scramjet flows have been performed using computational fluid dynamic (CFD) techniques, in conjunction with experimental studies in AFRL/RQH Research Cell 18 (RC18) and Research Cell 19 (RC19). Flow distortion is created in scramjet inlets during flight due to the effects of viscosity near the walls, the effects of shock waves caused by turning the flow, and by the interactions of the viscous boundary layers with shock waves. However, most fundamental scramjet experiments take place in direct-connect test facilities, without an inlet. To support the experimental study of distortion in these direct-connect facilities, CFD was used to design ground test hardware that would create shock waves and boundary layers consistent with flight inlets. Other studies were made on the interaction of these flow distortions with the fuel injection, mixing, and combustion. These studies provide the first detailed investigation of the interaction effects where detailed ground test data is available to validate the computational results. These results have provided key insights into the interaction effects, which will be used to guide the design of scramjet combustors that are tolerant of the anticipated distortion field.

15. SUBJECT TERMS
computational fluid dynamics, scramjet, inlet, combustor, distortion

16. SECURITY CLASSIFICATION OF:			17. LIMITATION OF ABSTRACT:	18. NUMBER OF PAGES	19a. NAME OF RESPONSIBLE PERSON (Monitor)
a. REPORT Unclassified	**b. ABSTRACT** Unclassified	**c. THIS PAGE** Unclassified	SAR	70	Mark A. Hagenmaier **19b. TELEPHONE NUMBER** (Include Area Code) N/A

Table of Contents

List of Figures

iii

List of Tables

1 Summary

This report documents the technical effort on Work Unit Q0E8/2308AI02, with a focus on the effect of flow distortion on fundamental scramjet flows. These studies have been performed using computational fluid dynamic (CFD) techniques, in conjunction with experimental studies in AFRL/RQH Research Cell 18 (RC18) and Research Cell 19 (RC19).

Flow distortion is created in scramjet inlets during flight due to the effects of viscosity near the walls, the effects of shock waves caused by turning the flow, and by the interactions of the viscous boundary layers with shock waves. However, most fundamental scramjet experiments take place in direct-connect test facilities, without an inlet. To support the experimental study of distortion in these direct-connect facilities, the first task was to utilize computational methods to design ground test hardware that would create shock waves and boundary layers consistent with flight inlets.

The technical effort also involved computational studies of the interaction of these flow distortions with the fuel injection, mixing, and combustion. These studies provide the first detailed investigation of the interaction effects where detailed ground test data is available to validate the computational results. These results have provided key insights into the interaction effects, which will be used to guide the design of scramjet combustors that are tolerant of the anticipated distortion field.

2   Introduction

Supersonic combustion ramjet (scramjet) engines are of interest to the Air Force for multiple applications, and therefore in multiple size classes ranging from small (about 10 lb of air per second) to medium (about 100 lb/s) to large (about 1000 lb/s). Development of these engines commonly involves several phases of experimental evaluation in close collaboration with computational fluid dynamics (CFD) simulations. A typical approach is to perform inlet-isolator component-level experiments on sub-scale models in low enthalpy freejet facilities, while combustor experiments are conducted in full-scale, high enthalpy facilities. Following these successful component tests, the integrated engine (inlet-isolator-combustor-nozzle) is evaluated in a freejet or semi-freejet (with portions of the inlet and/or nozzle removed) facility prior to flight testing.

In the direct-connect test environment, combustor testing is typically accomplished using a facility nozzle that is designed to produce a uniform, supersonic gas stream with one-dimensionally averaged flow properties that match the expected conditions at the engine throat (entrance to the engine isolator) in a flight vehicle. While this test environment offers substantial advantages over the freejet environment (reduced experimental complexity, potentially longer test duration, generally simplified test article design constraints, more flexible instrumentation options, etc.), direct-connect testing does not reproduce the highly distorted flow profile caused by oblique shocks generated in the scramjet inlet. This raises concerns that the performance and operability results obtained in direct-connect experiments may not be representative of the freejet and/or flight environments. Another consideration is that freejet testing of large scramjets is not possible in existing ground test facilities. Development of these large scale scramjets will likely proceed directly from direct-connect testing to flight. In that case, it may be critical to simulate the inlet distortion in the direct-connect testing as is done in turbojet engine development.

A method to simulate this distortion in an AFRL/RQH direct-connect scramjet test facility, Research Cell 22 (RC22), was demonstrated [1] for rectangular cross-section engines. The approach used was a nontraditional form of direct-connect testing, where a facility nozzle was used to generate the average conditions at a plane upstream of the engine throat where the conditions in the full engine are nearly uniform. Starting at this plane, the full engine geometry was replicated, causing the shocks generated within the direct-connect hardware to be consistent with those in the full engine. The hardware that was built to test this distortion generation approach was used for numerous combustor studies; however, a thorough comparison of the engine performance with and without flow distortion was not completed due to unexplained flow non-uniformities in the non-distorted case.

Section 4.1 describes improvements to the design of ground test hardware that provides shocks and boundary layers consistent with those expected in flight inlets, with application to AFRL/RQH Research Cell 18 (RC18). Creation of a realistic flow distortion within a direct connect setting is critical to obtaining complementary experimental data for comparison with the computational predictions.

Section 4.2 describes the investigations of an oblique shock wave impacting on jet injection into a supersonic crossflow. Injection normal to the wall is a common approach to obtain good fuel penetration, and the penetration characteristics with uniform inflows have been well characterized [2,3]. The present computational studies were carried out with a complimentary experimental study with the AFOSR efforts of Cam Carter to assess the impact of shocks on the fuel penetration and mixing.

Section 4.3 documents computational studies of cavity flameholders in the presence of distorted inflows. Cavities are often used to stabilize supersonic combustion by inducing separation within [4,5]. These studies were also performed in conjunctioin with the AFOSR efforts of Dr. Cam Carter to assess the impact of shocks on the cavity flowfields.

Large eddy simulation (LES) and direct numerical simulation (DNS) methods have shown success in predicting many turbulent flows, but are very expensive computationally for wall-bounded high Reynolds number flows, as the turbulent scales that need to be resolved by the grid become very small. Hybrid methods [6–8] have been developed to use LES for the majority of the flowfield and use RANS near solid surfaces, where the turbulent length scales are small.

The computational studies involve both steady state approaches using RANS simulations, as well as unsteady approaches using the hybrid LES/RANS simulations. For injection flows, RANS simulations have proved to be adequate for predicting penetration heights, but have not typically been as successful at predicting lateral spreading, vortical structures within plumes, or mixing within the core of injectant plumes [9–11]. RANS modeling of cavity flameholders have been performed regularly in the past [12,13] but only in recent years have computational resources allowed for the simulation of these flows with unsteady LES and LES/RANS methods.

3 Methods, Assumptions, and Procedures

3.1 REACT-MB for Hybrid LES/RANS and RANS Simulations

A hybrid LES/RANS method was developed at North Carolina State University's Aerospace Engineering CFD Lab [14] for use with their REACT-MB flow solver in hypersonic flow applications. It uses RANS as a near-wall method that smoothly transitions to LES in the boundary layer where the logarithmic layer deviates from the wake law in a time-averaged sense. This method has been successful in predicting Mach 2 crossflow cases with air, helium and ethylene injection [10].

The REACT-MB hybrid LES/RANS formulation was used for some of the simulations shown in this work. The hybrid method [15] combines a Menter BSL RANS model near the wall with a Smagorinsky subgrid model away from the wall. The transition from LES to RANS is accomplished by a blending function based on the ratio of the closest wall distance to a modeled form of the Taylor microscale. An unsteady inflow condition was provided using a recycling and rescaling routine which is detailed in earlier work [15]. RANS simulations with REACT-MB utilized the Menter BSL model for the turbulent fluxes. Inviscid fluxes are discretized using Edwards' Low-Diffusion Flux-Splitting Scheme (LDFSS) [16] and viscous and diffusive fluxes used second-order central differences. The Piecewise Parabolic Method (PPM) of Colella and Woodward [17] was used to extend LDFSS to higher order accuracy.

3.2 CFD++ for RANS Simulations

RANS simulations were performed using version 10.1 of the CFD++ code, a general-purpose CFD tool developed by Metacomp Technologies [18]. CFD++ uses a finite-volume numerical framework, with multi-dimensional Total Variation Diminishing (TVD) schemes and Riemann solvers for accurate representation of supersonic flows. Several types of Riemann solver are available; the Harten-Lax-van Leer-Contact (HLLC) Riemann solver with minmod flux limiting was used in the simulations described here. Multi-grid acceleration is available to provide a fast and accurate solution methodology for both steady and unsteady flows. A variety of one-, two-, and three-equation turbulence models are available for RANS calculations, along with LES and hybrid RANS/LES options. In all the cases presented here, turbulence was modeled using the two-equation cubic $k - \epsilon$ model. This model has nonlinear terms that account for normal-stress anisotropy, swirl, and streamline-curvature effects. At solid surfaces, an advanced two-layer wall function with equilibrium and nonequilibrium blending was employed to reduce grid requirements. Turbulent species mixing is modeled using a constant turbulent Schmidt number (Sc_t) equal to 0.5 while the turbulent heat flux is modeled using a constant turbulent Prandtl number (Pr_t) of 0.9. Structured grids were used for the present study, although CFD++ supports both structured (hexahedral) and unstructured (prism and tetrahedral) grids. A Message Passing Interface (MPI) is used to take advantage of modern parallel-processing computers. The finite rate chemistry is

modeled using the Taitech/Princeton TP2 kinetics mechanism [19], which models 22-species ethylene combustion.

4   Results and Discussion

The individual research areas are described below. The first subsection documents the development of a unique procedure that creates flight-like distortion in a direct-connect test facility. The second subsection describes LES/RANS analysis of the effects of shocks on injection into a supersonic crossflow. The third focuses on LES/RANS analysis of shock effects on nonreacting flows in cavity flameholders and RANS analysis of reacting flows in cavity flameholders.

4.1 Distortion Generation in Direct-Connect Facilities

Prior work [1] aimed to develop representative distortion for the AFRL/RQH direct-connect combustor hardware in Research Cell 22 (RC22), with 42.4 mm high and 228.6 mm wide cross-section, and a throat Mach number of approximately 2.5. That study focused on understanding the performance impacts of the flow distortion on isolator performance. RC22 had limited capabilities for optical diagnostics, and was unable to support a more fundamental study of the impact of flow distortion. The present work applies a similar approach to create a representative distortion for AFRL/RQH direct-connect combustor hardware in Research Cell 18 (RC18), which has the capability to support advanced optical diagnostics in the isolator section. The cross-section of RC18 is 38.1 mm x 101.6 mm, and a facility nozzle exists which provides uniform flow with a throat Mach number of approximately 2.18. Figure 1 shows a diagram of the flow structure in a planar compression inlet. An expansion fan is generated by the turning of the body wall at the throat (called the shoulder), but has been excluded in this diagram. In each of the flow regions upstream of the engine throat (noted as 0, A, B, and C in the figure) the flow properties are nearly constant. In a traditional direct-connect study, a facility nozzle is used which matches the average condition at the engine throat.

An empirical model for isolator performance [20] in rectangular ducts is expressed as:

$$\frac{(M_1^2 - 1)\left(\frac{S}{H}\right)\text{Re}_\theta^{0.2}}{\sqrt{\theta/H}} = 50\left(\frac{p}{p_1} - 1\right) + 170\left(\frac{p}{p_1} - 1\right)^2 \tag{1}$$

This shows that isolator pressure rise is dominated by the incoming Mach number M_1, and the momentum thickness θ. Therefore, matching the average Mach number and the momentum thickness is a goal in the development of the distortion generator. To understand the impact of flow distortion on isolator performance, it is desired to compare a full engine, a direct-connect engine without inflow distortion (i.e. the traditional approach), and a direct-connect engine with inflow distortion. All three
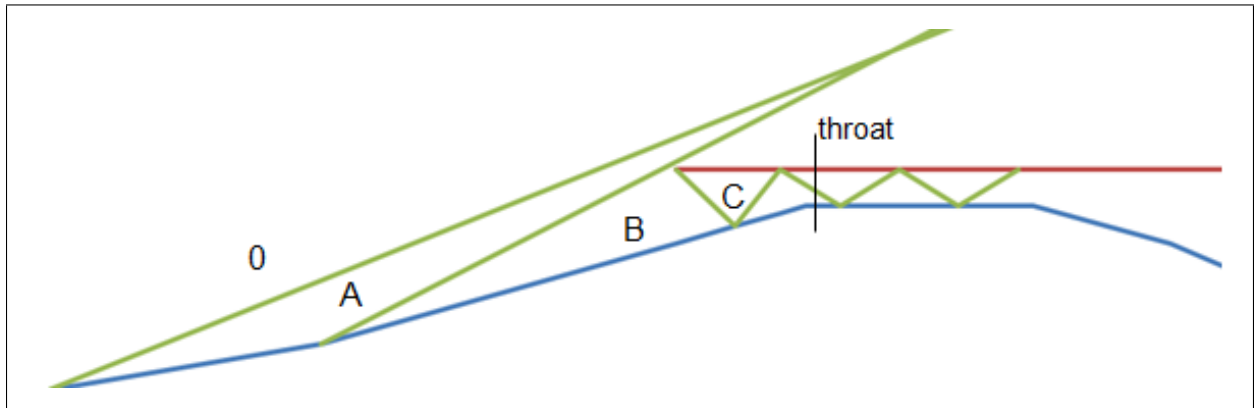
Figure 1: Planar Compression Scramjet Flow Structure
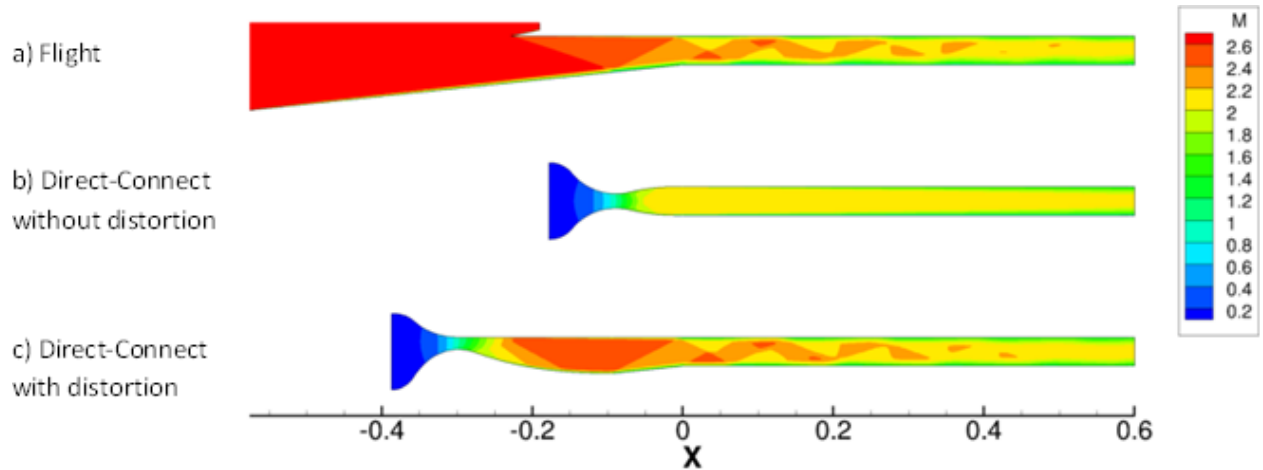
Figure 2: Center Plane Mach for Flight and Direct-Connect Conditions
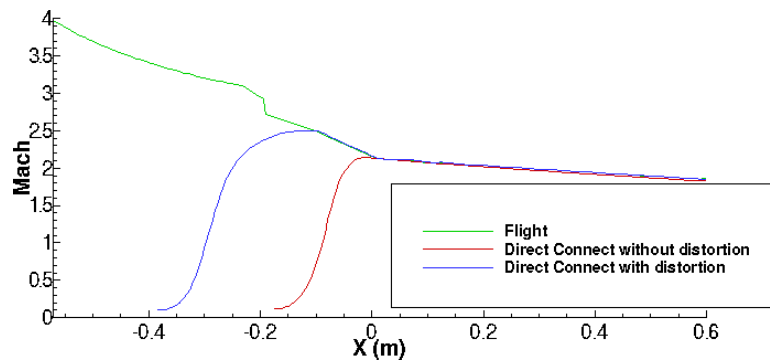
Figure 3: Average Mach for Flight and Direct-Connect Conditions

testing modes are investigated in the current study using RANS CFD modeling tools, and the two direct-connect modes will be studied in a future experimental study in RC18.

4.1.1 Flight Mode

A generic inlet is considered for this study, which employs a single 6-degree forebody turning angle, and a cowl that turns the flow back to the axial direction. This is obviously not an optimized inlet, but the cowl turning angle, which dictates the strength of the internal shocks that create the flow distortion, is representative of planar compression scramjets. The Mach number and angle of attack of the flight inlet were varied such that the average Mach number at the throat was 2.18, to be consistent with an existing facility nozzle available for RC18. For the present study, a flight condition of Mach 4, dynamic pressure of 95.7 kPa (2000 psf), and an angle of attack of 9.2 degrees provided the desired throat Mach number of 2.18. Figure 2 shows the Mach distribution on the center plane, while the Figure 3 shows the average Mach for each streamwise location. Figure 4 shows the pressure distribution on the centerplane, while Figure 5 shows the average pressure for each streamwise location.

8
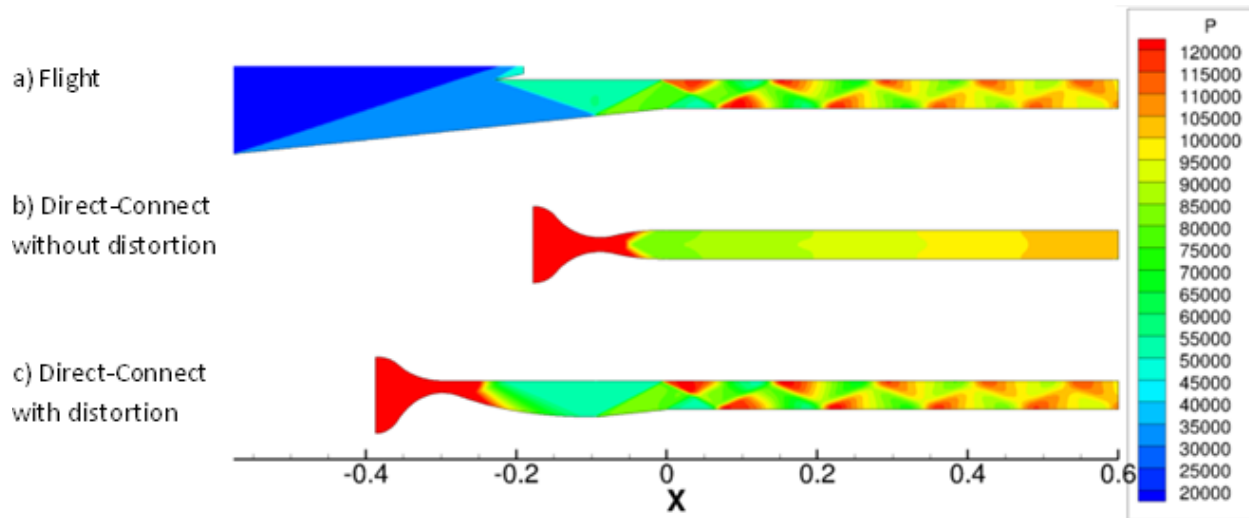
Figure 4: Center Plane Pressure for Flight and Direct-Connect Conditions
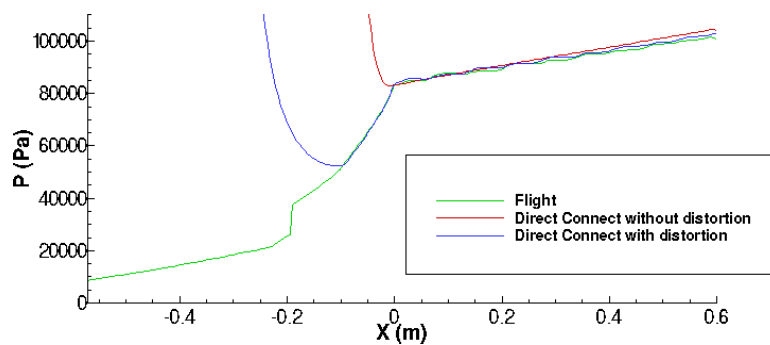
Figure 5: Average Pressure for Flight and Direct-Connect Conditions

9
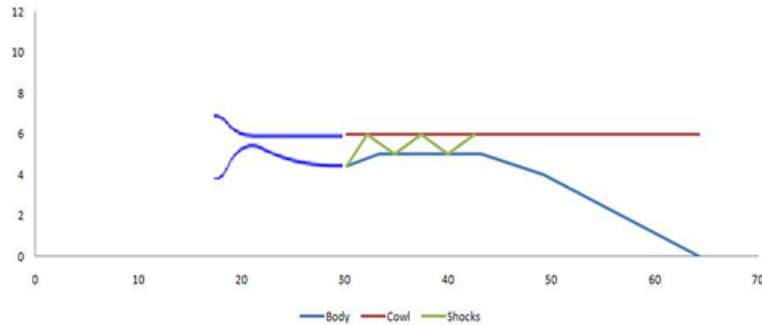
Figure 6: Schematic of Distortion Generator Configuration

4.1.2 Nondistorted Direct-connect Mode

An existing RC18 facility nozzle, which produces near-uniform flow, was analyzed for consistency with the flight inlet. The nozzle area ratio is approximately 2.0. At conditions consistent with Mach 4 flight at a dynamic pressure of 95.7 kPa (2000 psf), the average Mach number at the engine throat is 2.18. This throat condition is consistent with the generic flight inlet. Figure 2 and Figure 4 shows the Mach and pressure distribution on the center plane for the nondistorted direct-connect mode. Figure 3 and Figure 5 show that the average Mach and pressure are consistent with the flight inlet from the engine throat through the end of the isolator.

4.1.3 Distorted Direct-connect Mode

The design of the distortion generator hardware proceeded from the CFD results for the flight inlet. The procedure developed in Reference [1] results in a new facility nozzle that generates the flow properties in region C, where the flow is parallel to the cowl. For the generic inlet at the matching flight condition, the Mach number in region C is approximately 2.50, and the shock that separates region C from region D is generated 94 mm upstream of the engine throat. That location defines the start of the compression region of the distortion generation device. A method-of-characteristic procedure with boundary layer corrections was used to define a nozzle that provides the Mach 2.50 conditions. Figure 6 shows a schematic of the distortion generator configuration. The facility nozzle that generates Mach 2.50 flow and the compression section from the shock reflection point 94 mm upstream of the throat will likely be constructed as a single unit for the planned experimental program. Figure 2 and Figure 4 show the Mach and pressure distribution on the center plane for the distorted direct-connect mode, and show similar shock structures as the flight inlet. Figure 3 and Figure 5 show that the average Mach and pressure are consistent with the flight inlet from the shock reflection point 94 mm upstream of the engine throat through the end of the isolator.

Comparisons of body and cowl centerline wall pressure of the three testing modes are included in Figure 7 and Figure 8. Excellent agreement between the flight and distorted direct-connect modes is seen, showing a similar oscillating pressure caused by the

10
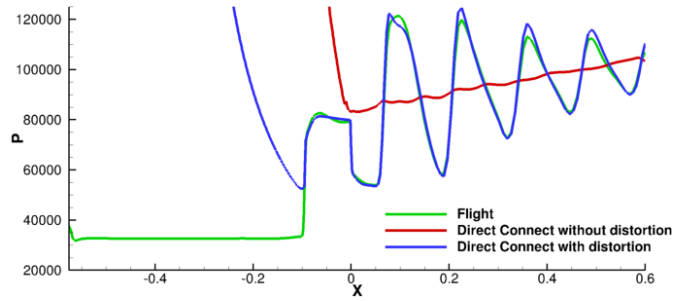
Figure 7: Body-Side Centerline Wall Pressure Comparison
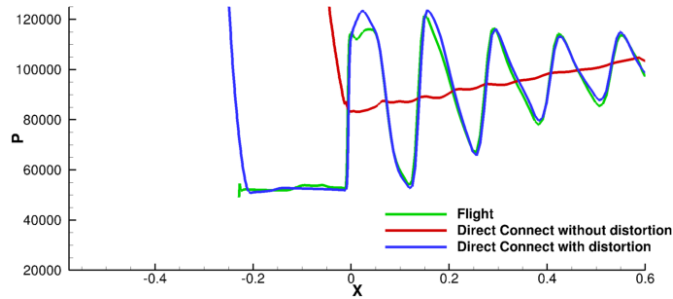
Figure 8: Cowl-Side Centerline Pressure Comparison

reflections of the inlet shock and shoulder expansion. As expected, the nondistorted direct-connect pressures show a smoothly increasing pressure caused by the supersonic deceleration of the flow due to wall friction.

The preceding data shows how well the distorted direct-connect mode matches the average conditions and shock structure of the flight mode. However, models such as Equation 1 also relate isolator performance to boundary layer parameters such as momentum thickness. Computations of momentum thickness on the centerline are shown in Table 1. The direct-connect without distortion mode is seen to have thinner boundary layers than the flight, while the direct-connect with distortion has values closer to the flight values.

However, the computation of the momentum thickness has some ambiguity for internal distorted flows due to an ill-defined edge condition. Another approach to comparing boundary layer parameters is to compare wall shear stress. Comparisons of the wall shear stress on the body and cowl centerlines are shown in Figure 9 and Figure 10. It is seen that the distorted direct-connect mode more closely matches the wall shear stress

Table 1: Momentum Thickness on Centerline at Engine Throat

Mode	θ (body)	θ (cowl)
Flight	0.638 mm	0.476 mm
Direct-Connect without distortion	0.226 mm	0.226 mm
Direct-Connect with distortion	0.512 mm	0.693 mm

11
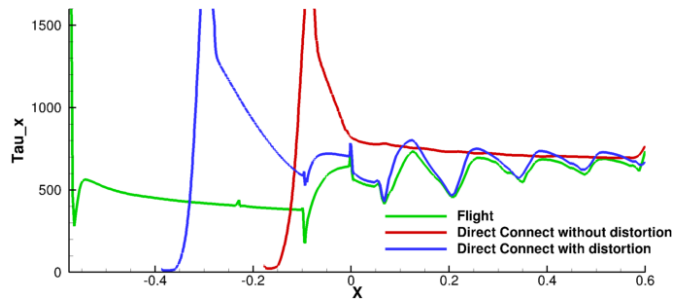
Figure 9: Body-Side Centerline Wall Shear Stress Comparison
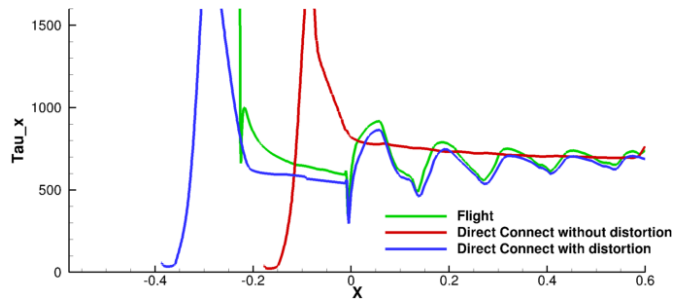
Figure 10: Cowl-Side Centerline Shear Stress Comparison

expected in flight, in agreement with the momentum thickness results.

Figure 11 shows Mach number on the centerline just downstream of the throat. The slope of the Mach profiles at the wall indicates that the wall shear is similar for the distortion mode and the flight mode, but the overall boundary layer thickness and shape are still somewhat different.
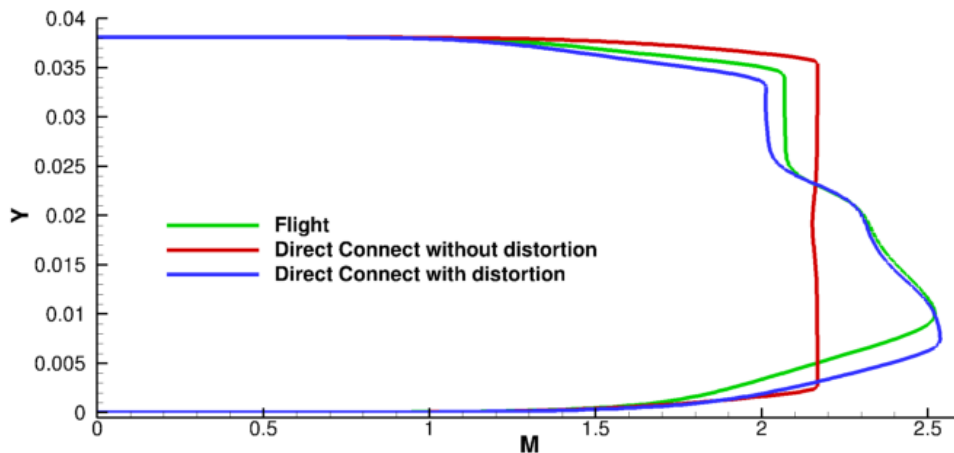
Figure 11: Mach Distribution on Center Plane Just After Throat

12

4.2   Shocked Injection

An aspect of scramjet physics that needs further investigation is the role of flow distortion caused by oblique shock from the cowl in scramjet flows. In typical direct connect wind tunnel facilities, the flow is nearly uniform coming out of the facility nozzle – completely missing the impact of this cowl shock. Studies have shown [21,22] that these shocks have significant impact on mixing and plume structures. This section discusses the experimental study of an oblique shock impinging downstream of a normal injector, followed by a description of the hybrid LES/RANS simulations and comparison to the experimental observations.

An experimental investigation of the impact of oblique shock waves on normal jet injection of air has been conducted to complement the computational studies being performed. The tunnel conditions and jet conditions mimic those used in prior studies [2,3] of normal jet injection. A single circular jet with a jet diameter (D) of 3/16 inch was located in the bottom wall of the tunnel, approximately 5.9 inches from the end of the Mach 2 facility nozzle of Research Cell 19 at the Air Force Research Laboratory [23]. On the upper wall, a beveled plate was mounted, which could be translated axially. The leading bevel turned the flow by either 5 or 7 degrees, before turning back parallel to the lower wall. The shock generator thickness was 3/8 inch. During calibration runs, a shadowgraph system was used to verify the position of the shock relative to the injector.

Following the calibration runs the shadowgraph system was replaced by an nitrous oxide planar laser-induced fluorescence (NO-PLIF) system. NO-PLIF images were obtained on spanwise planes located at 0, 2.5, 5, 10, 15, 20 and 25 jet diameters downstream of the injector. The NO-PLIF imagery has the advantage of providing snapshots of fluorescence (which is a good analog for injectant mass fraction for limited temperature ranges). This imagery provides detailed information on the normal and lateral spreading characteristics of the ethylene jet.

Hybrid LES/RANS and RANS simulations of normal sonic ethylene injection with an oblique impinging shock downstream of the injector have been performed. The theoretical waves formed by the 5-degree shock generator can be found in Figure 12. As can be seen a pair of shocks and expansion fans emanate from the shock generator. The oblique shock condition formed by the shock generators were imposed by altering the inflow condition to be consistent with the conditions downstream of an oblique shockwave from a five or seven degree shock generator on the top wall as they would be in the experiment. Only the oblique shock is imposed in the numerical investigations and no expansion waves are introduced. The expansion waves would only impact the injection plume downstream of most of the region of interest and it is thought that they would have minimal impact on mixing. The oblique shock from the 5-degree shock generator interacts with the injection plume between the $x/D = 2.5$ and $x/D = 5$ data collection planes and strikes the bottom wall at approximately $x/D = 8.4$. The oblique shock caused by the 7-degree shock generator strikes the bottom wall at approximately $x/D = 5.25$.
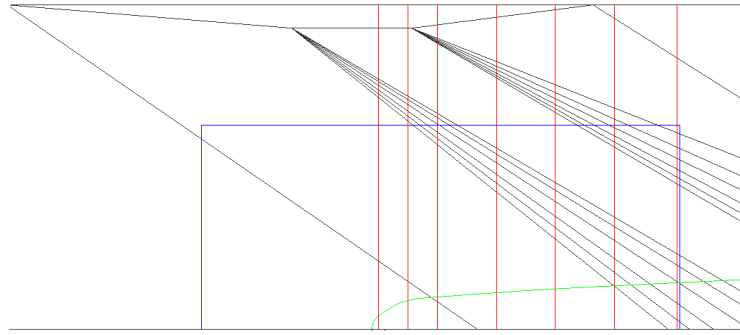
Figure 12: Shocked Injection Analytical Wave Diagram (Interactions Not Shown)

The vertical red lines indicate data planes at which cross-plane NO-PLIF data was gathered experimentally and compared with CFD results in this work. The blue rectangle indicates the computational domain in X and Y.

RANS simulations for a momentum flux ratio (q) of 1.5 have been performed for injection with no shock generator and then with the 5- and 7-degree shock generator as described above. Center-plane Mach number contours for these simulations can be seen in Figure 13. The red contour line denotes zero axial velocity and implies a significantly larger boundary layer separation for the 7-degree shock generator case than the other two simulations.

Hybrid LES/RANS simulations were performed to better capture the unsteady mixing and the impact of the shock impingement. Time-averaged center-plane contours of Mach number can be seen in Figure 14. The contours look similar to the RANS contours which is consistent with other mixing simulations in that the centerplane flow characteristics are well-predicted by RANS, but off-center characteristics are not. Mixing within the fuel plume shows the biggest advantage of LES/RANS over RANS methods. Figure 15 shows the same plane with crossflow species density contours so that the wave structure as well as the injection plume can be discerned. The sonic line is shown in red and reveals that nearly all of the plume is subsonic in the case with the 7-degree shock generator. This confirms that there is indeed more separation in the 7-degree shock generator case that than the 5-degree case. Since there was limited wind tunnel time, these simulation results were used as evidence that only the 5-degree shock generator should be used, as the 7-degree shock generator introduces too much separation on the bottom wall.

Side-view high-speed shadowgraph imagery was collected and the time average of the q = 1.5 case can be seen in Figure 16. Since the 5-degree generator was used in the experiment, the oblique shockwave and expansion wave interact with the injection plume further downstream than in the 7-degree theoretical diagram shown in Figure 12. It is also notable that the upstream expansion wave hardly interacts with the region of interest. The view outlined in red in Figure 16 is recreated numerically in Figure 17 by the LES/RANS simulation. The major flow features are all simulated accurately including the separation and bow shocks upstream of the fuel injection. The experiment shows a shock that is reflected off of the bottom wall that does not appear in the CFD.
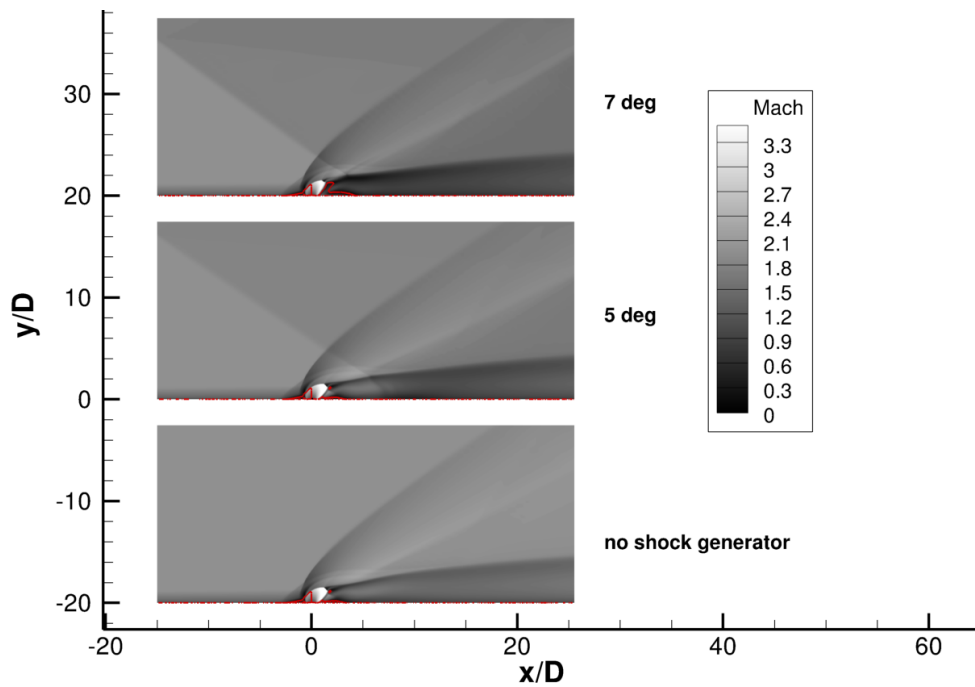
Figure 13: Mach Number Contours for Centerline without Shock Generator and with 5 and 7-Degree Shock Generators Using RANS

Zero axial velocity line shown in red.
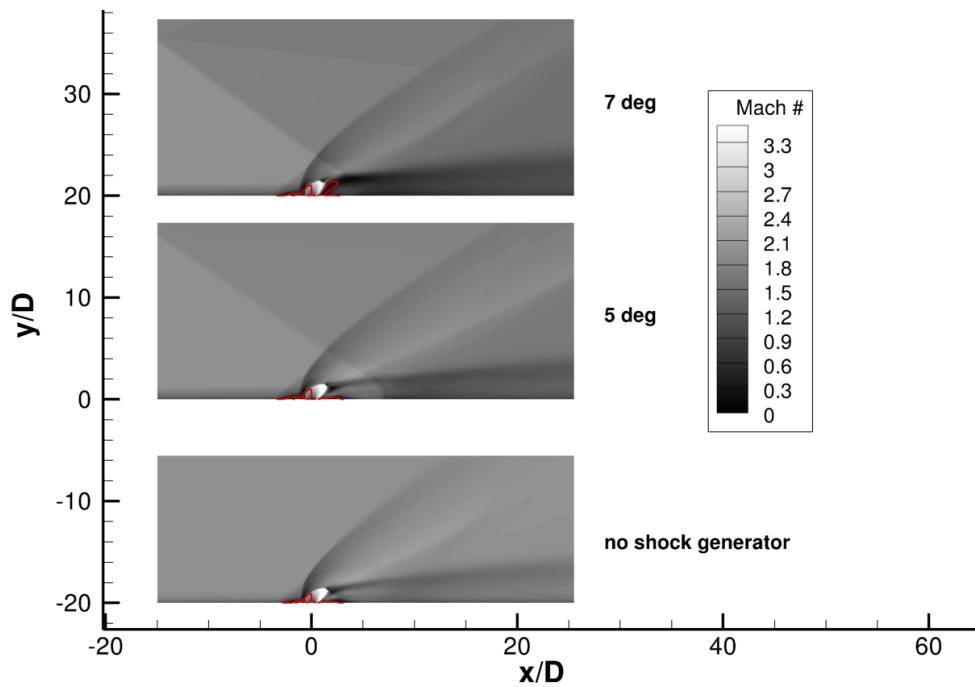
Figure 14: Mach Number Contours for Centerline without Shock Generator and with 5 and 7-Degree Shock Generators Using LES/RANS

Zero axial velocity line shown in red.

15
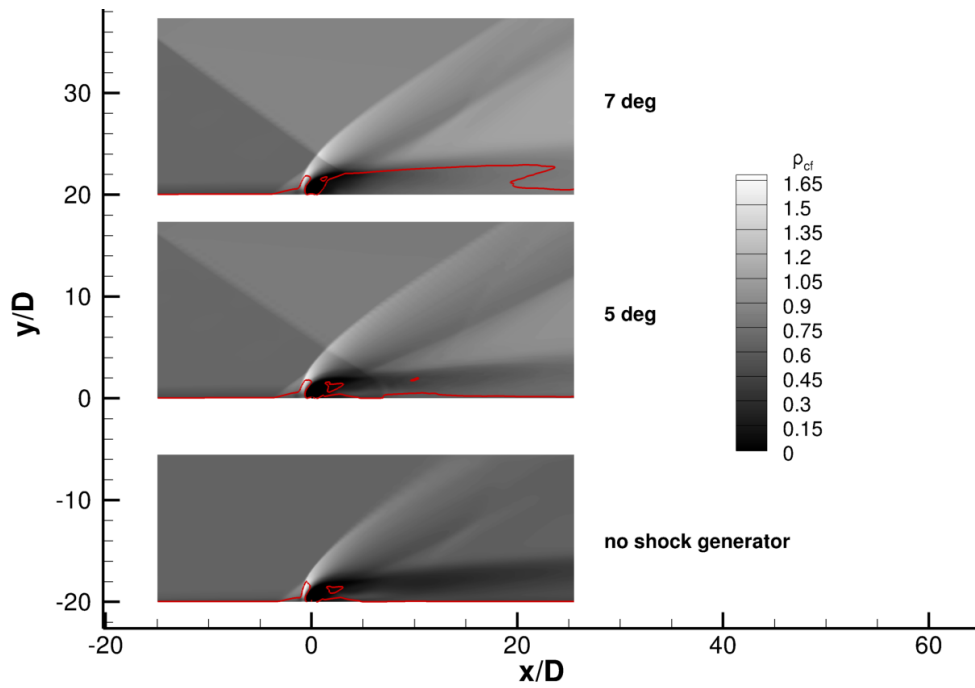
Figure 15: Crossflow Air Species Density Contours for Centerline without Shock Generator and with 5 and 7-Degree Shock Generators Using LES/RANS

Sonic line shown in red.
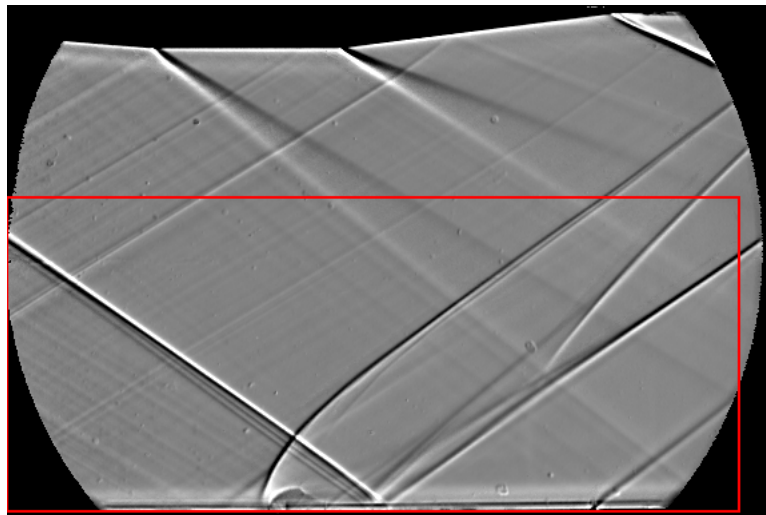
Figure 16: Time-Averaged Experimental Shadowgraph for q=1.5 Air Injection with 5-Degree Shock Generator

X-Y domain for CFD simulations outlined in red.

16
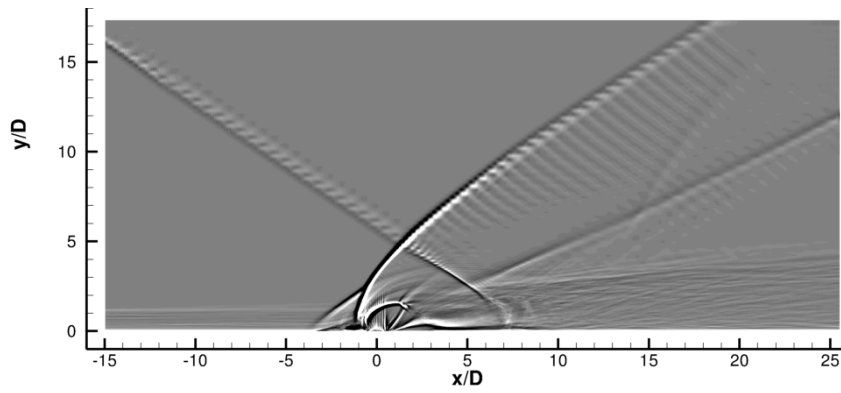
Figure 17: Time-Averaged Numerical Shadowgraph for q=1.5 Ethylene Injection
LES/RANS with 5-Degree Shock Generator
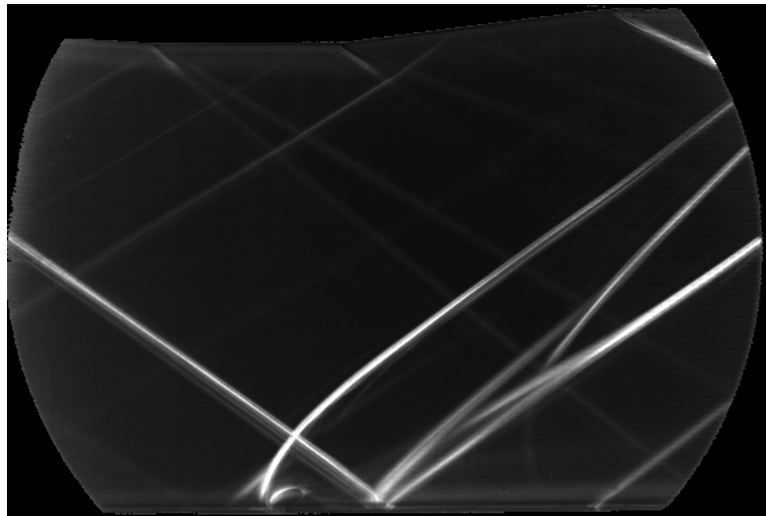
Figure 18: Standard Deviation of Experimental Shadowgraph for q=1.5 Air Injection
with 5-Degree Shock Generator

(a) x/D=5   (b) x/D=10   (c) x/D=25
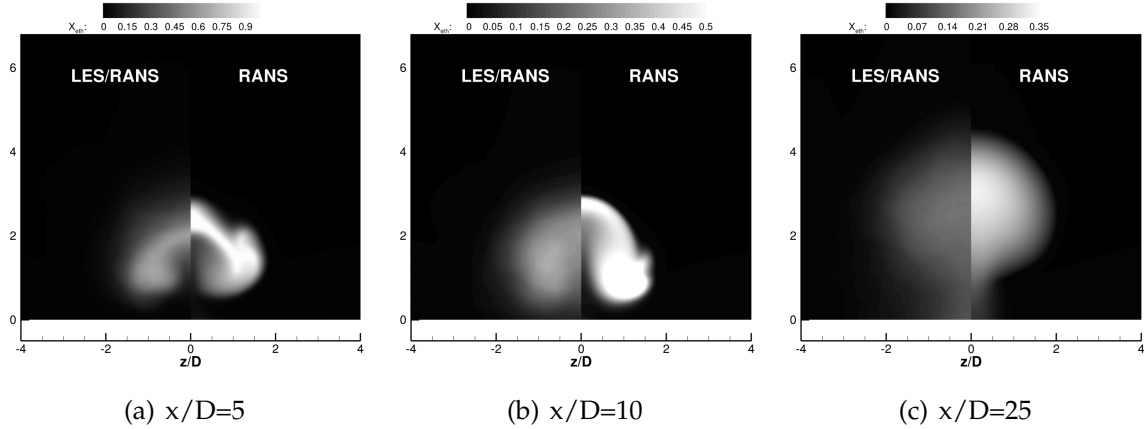
Figure 19: Time-Averaged LES/RANS and RANS Cross Plane Contours of Injectant Mass Fraction for q=1.5, 5-Degree Shock Generator Case

(a) x/D = 5   (b) x/D = 10   (c) x/D = 25
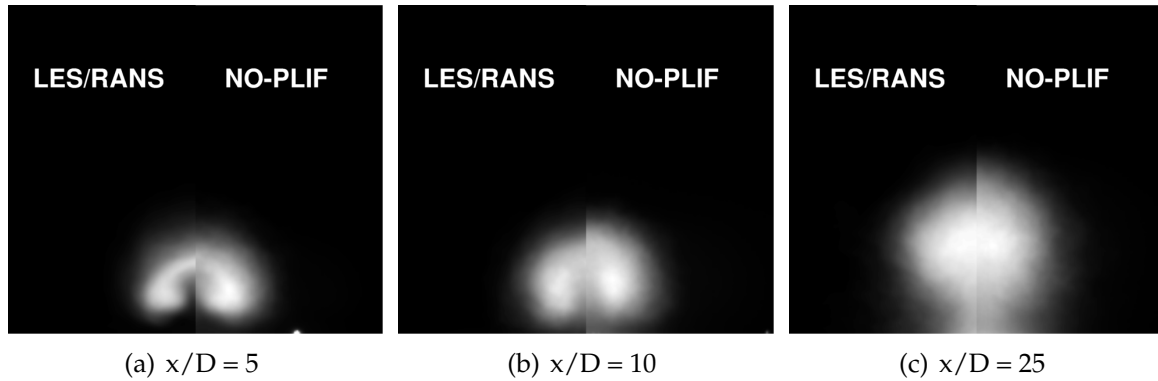
Figure 20: LES/RANS Time-Averaged Cross Plane Contours of Injectant Mass Fraction Compared with NO-PLIF Time Average for 5-Degree Shock Generator Case

This appears because the experimental shadowgraph is formed by the density changes across the entire width of the tunnel, whereas the numerical shadowgraph is only determined by the center plane. In the center plane the reflected shock occurs away from the wall because of the injection plume. The experimental standard deviation plot shown in Figure 18 shows that there is not much movement of the shocks involved in the system.

Earlier studies [10, 24] have shown that the REACT-MB LES/RANS model is able to capture the shape and mixing within plumes better than RANS simulations. A comparison of RANS to LES/RANS simulations can be seen in Figure 19. The RANS and LES/RANS simulations look strikingly different in their shape and mixing, though the height of the plumes and separation from the bottom wall is similar. The LES/RANS simulation looks very similar to the experimental NO-PLIF imagery seen in Figure 20. The standard deviation imagery seen in Figure 21 again shows that the LES/RANS method did well to simulate the unsteady motion of the plume.

In order to gauge the impact of the shock generator on the mixing of the flow, Figure 22

18

(a) x/D = 5 (b) x/D = 10 (c) x/D = 25
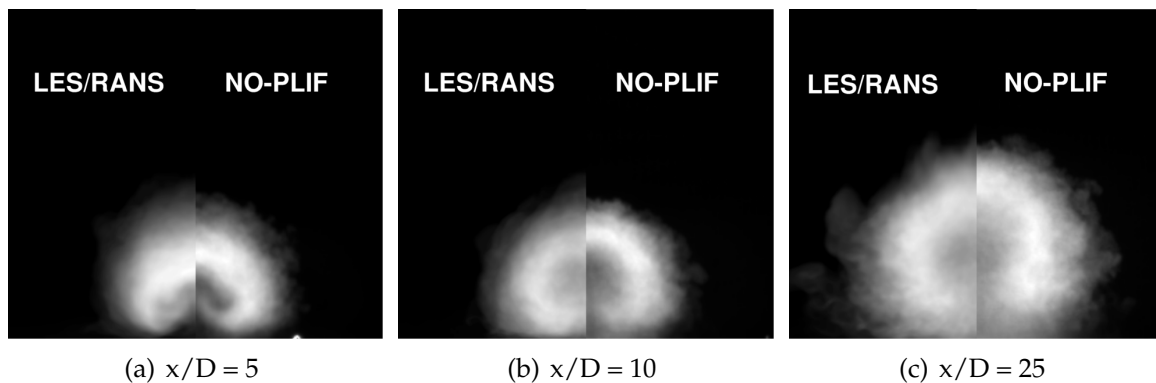
Figure 21: Standard Deviation of LES/RANS Cross Plane Contours of Injectant Mass Fraction Compared with the Standard Deviation of NO-PLIF Imagery for 5-Degree Shock Generator Case

(a) x/D=5 (b) x/D=10 (c) x/D=25
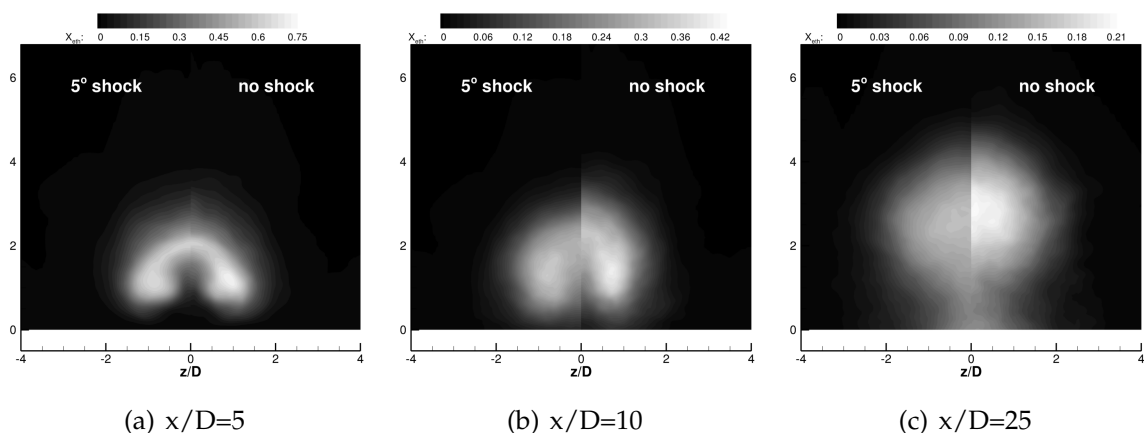
Figure 22: Time-Averaged Cross Plane Contours of Mass Fraction with a 5-Degree Shock Generator and No Shock Generator

(a) x/D=5 (b) x/D=10 (c) x/D=25
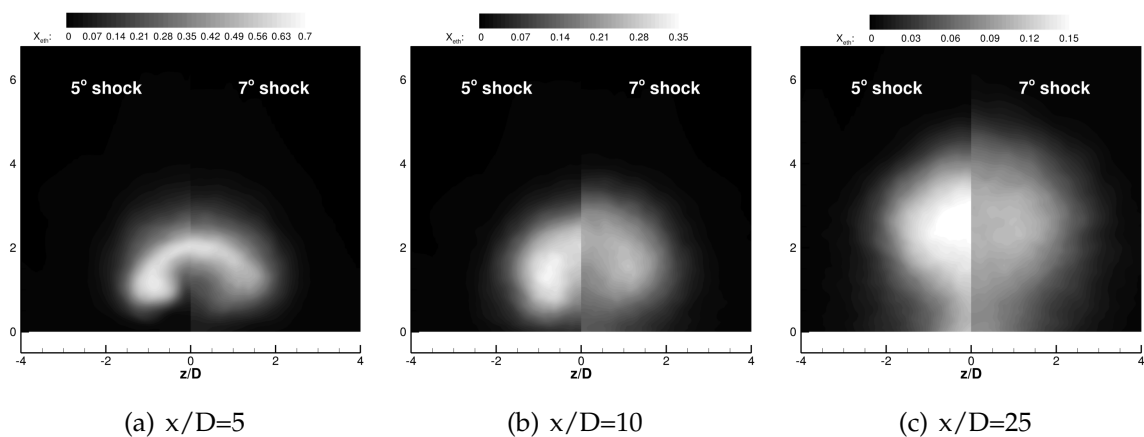
Figure 23: Time-Averaged Cross Plane Contours of Injectant Mass Fraction with 5- and 7-Degree Shock Generator

19
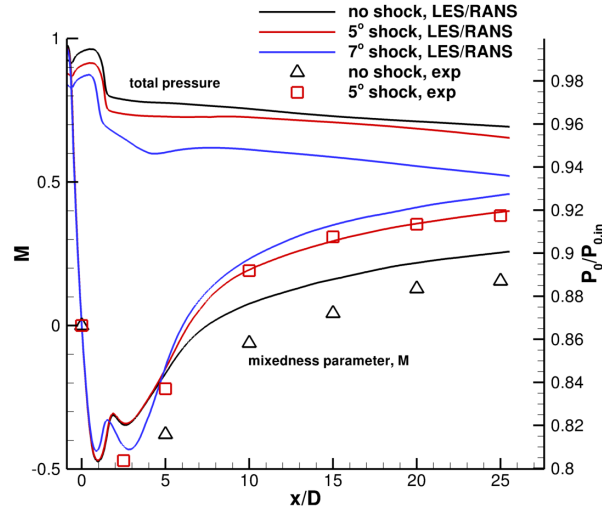
Figure 24: Time-Averaged and Experimental Mixedness Parameter and Computational Total Pressure Losses Averaged Over Each Streamwise Plane

shows contours of time-averaged injectant mass fraction with and without the 5-degree shock generator using LES/RANS. Downstream of the shock impingement ($x/D = 10$ and $x/D = 25$ stations in this case), the injection plume is closer to the wall than the undistorted case. There is also more mixing in the simulation with the shock generator than without. Both of these impacts are predictable because the flow is slowing down allowing for more time for mixing as well as the pressure increase from the shock is keeping the plume closer to the wall. The simulation of the 7-degree shock generator case is compared to the 5-degree shock generator case in Figure 23. This shows that the 7-degree shock generator causes substantially more mixing than the 5-degree case. This falls in line with the reasoning that a stronger shock slows the flow down more allowing for more mixing. However, the plume itself is further from the wall than the 5-degree case even though the pressure jump from oblique shock would be greater for the 7-degree shock generator. It is theorized that this is due to the large separation seen in Figures 14 and 15.

In order to better quantify the impact of the shock generators on mixing, the mixedness parameter as defined by Fric [25] has been calculated for the LES/RANS simulations:

$$M = 1 - \frac{[\int |c - \bar{c}| \, dA]}{[\int |c - \bar{c}| \, dA]_{x/D=0}} \tag{2}$$

where c is time-averaged mixture fraction and $\bar{c}$ is the mixture fraction averaged over a given plane for the time-averaged solution. This method was also applied to the intensity values from the averaged NO-PLIF imagery for the 5 degree shocked and unshocked case for $q = 1.5$. The mixedness parameter for the experimental and computational data are compared in Figure 24. It can be seen from this plot that while there is a fairly large shift in mixedness between the case with no shock generator and

20

the one with a 5-degree shock generator, there is not much of an increase in mixedness when the 7-degree generator is used. But, when the 7-degree shock generator is used, a large drop in total pressure is seen – illustrating the downside of using shocks to increase mixing within a scramjet.

4.3   Shocked Cavity

Cavities are often used to provide a stable flame for supersonic combustion by inducing separation within [4,5]. The presence of a cavity downstream of a flush wall injector increases flow residence time, allowing for greater time for mixing and combustion. Steady-state numerical investigations of cavity flameholders have been performed regularly in the past using steady-state methods [12,13] but only in recent years have computational resources allowed for the simulation of these flows with unsteady LES and LES/RANS methods. In addition, the impact of flow distortion caused by oblique shocks from the cowl in scramjet flowpaths is of interest. This section discusses the impact of an oblique shock impinging in the region of a cavity flameholder. For mixing flows, computational studies were performed with both RANS and hybrid LES/RANS, while only RANS was used for combusting flows.

An experimental investigation of the impact of oblique shock waves on fuel injection in the cavity region was conducted to complement the computational studies being performed [26]. A single flush wall injector was located in the bottom wall of the tunnel a half inch upstream of the ramped cavity, with a 2.5° divergence starting upstream of the injector and cavity as seen in Figure 25. The 2 by 6 inches, Mach 3 configuration of Research Cell 19 (RC19) at the Air Force Research Laboratory Facility [27] was used. For these mixing flows, the total temperature and pressure were approximately 300K and 1.2 MPa, respectively. On the upper wall, a shock generator wedge was mounted as seen in Figure 25, and could be translated axially. The shock generator could be traversed three inches axially, which allowed the study of multiple shock impingement locations, from upstream of the injector to the middle of the cavity region. Three wedges seen in Figure 26 were fabricated and two wedges were tested, with deflections of 6.1° and 7.7° (the 5° wedge was not used due to irregularities in fabrication). The simulations focused on the 7.7° wedge.

Numerous diagnostics were used during the experiments. A shadowgraph system was used to calibrate the positioning of the shock generator as well as record the basic shock structures of the different configurations. For the noncombusting runs, NO-PLIF was used to record snapshots of injectant along spanwise planes. This imagery provided detailed information on the normal and lateral spreading characteristics of the non-reacting air jet. Ice crystal illumination using Mie scattering techniques were recorded as well for the low temperature cases. These measurements provide snapshots that are similar to crossflow temperature measurements and can be used as another way of visualizing the flow field shock structures. These proved important in the 7.7° wedge case because no shadowgraph imagery was performed for that wedge.

4.3.1   Nonreacting Flow Cases

In order to better understand the flow features of the cavity flameholder, it is first instructive to examine the flow structures far off-center in this flow outside of the influence of injection. To identify the different shock waves for each of the three cases, contours of static pressure seen in Figure 27 are analyzed to make a simplified wave
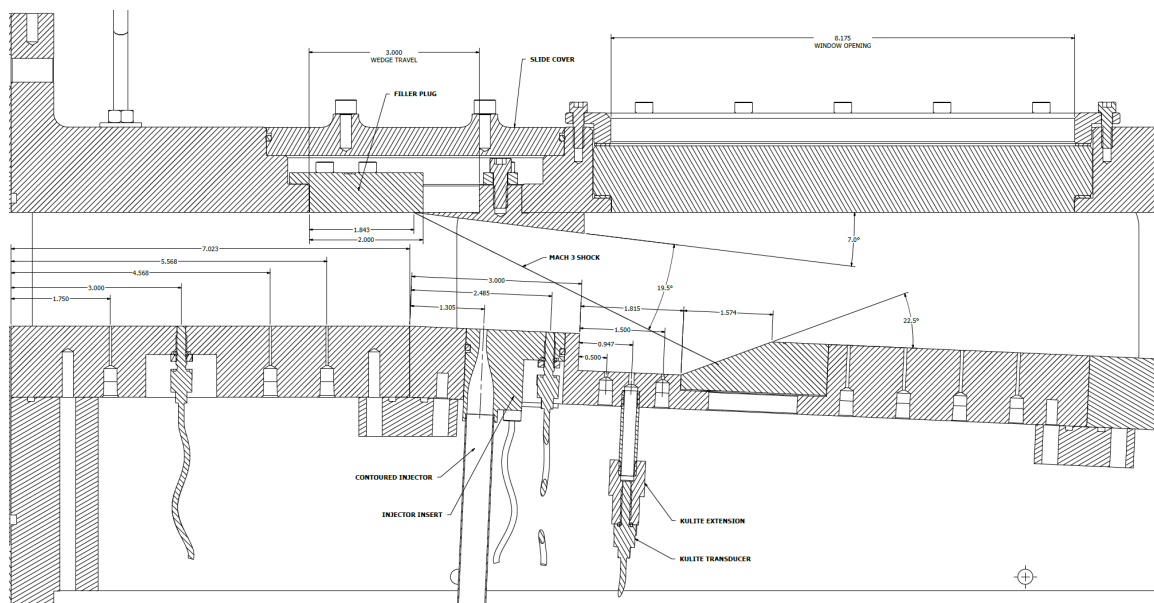
Approved for public release; distribution unlimited.

Figure 25: Schematic for Experiment with 7° Shock Generator in the Shock-On-Cavity Position

Units are inches. Injector block is reversed in the present experiment such that the injector is 0.5 inches upstream of the cavity.

diagram for the waves relevant to the cavity mixing (Figure 28). Figure 29 shows the Mach contours at this location.

There are three main types of shocks seen in the flow field away from the injector. The shock labelled S1 is the shock formed by the shock generator. The shock labelled S2 is formed by the separation of the boundary layer just upstream of the cavity. This phenomenon can be seen more clearly in the Mach contours in Figure 29. The No-Shock case doesn't show a separation upstream of the cavity thus S2 isn't present for that case. For the Shock-On-Jet case, there is a small shock-induced separation which causes a shallow, weak S2 shock that is also slightly turned by the expansion fan. For the Shock-On-Cavity case, the shock hits in the middle of the cavity and causes a larger separation upstream of the cavity causing a steeper and stronger S2 shock. The S3 shock is what is often referred to as a cavity close-out shock. It is caused by the turning of the flow caused by the ramp at the downstream end of the cavity. For the No-Shock case this is a straightforward interaction with a S3 shock formed that corresponds to the small blockage formed by the cavity closeout and its associated turning of the flow. For the Shock-On-Jet case the S3 shock is more severe than the others because the turning angle is more sharp than the other two cases. This is because S1 in this case causes the shear layer to be pushed toward the bottom wall, thus making the flow make a more severe turn at the cavity closeout. It is also clear that the expansion fan turns S2 and S3 slightly where they interact.

A contour plot of flow angle in a plane far from the centerplane (measured relative to the 2.5° divergence angle of the bottom wall) can be seen in Figure 30 with the black line

23
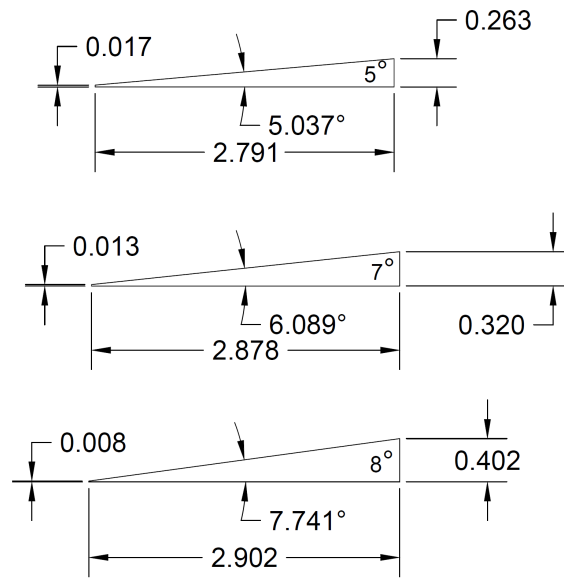
Figure 26: As-Built Wedge Shock Generators

Measurements all shown in inches. Nominal design wedge angles were 5, 7 and 8 degrees.
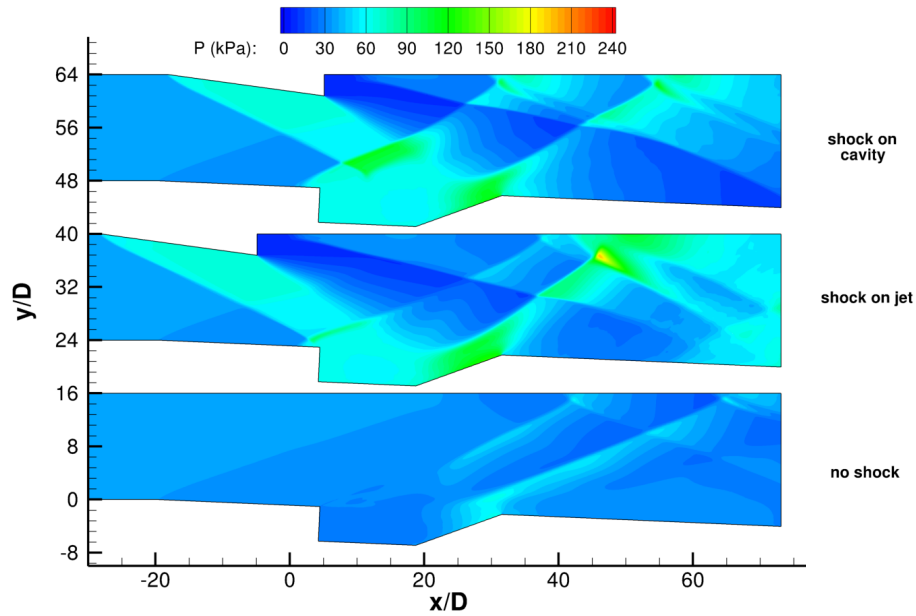
Figure 27: Contours of Time-Averaged Static Pressure at z/D = -11.9
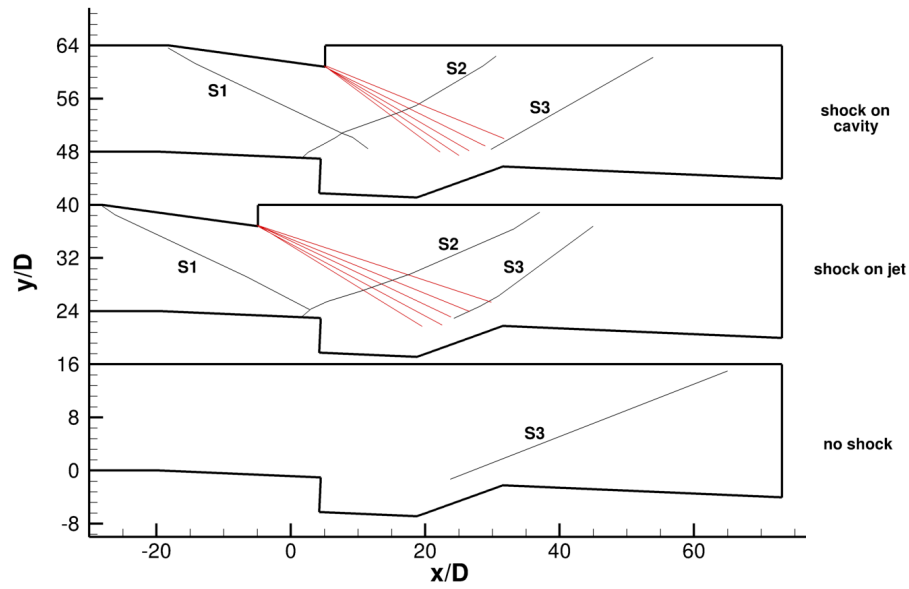
Figure 28: Wave Patterns Important to Cavity Mixing

Shocks in black, expansion fan in red.
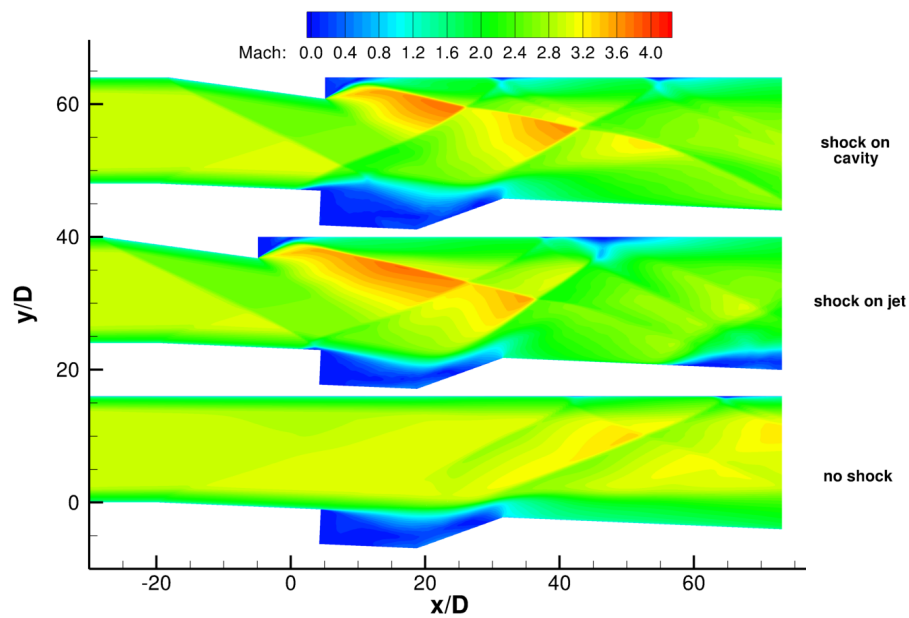
Figure 29: Contours of Time-Averaged Mach Number at z/D = -11.9

25
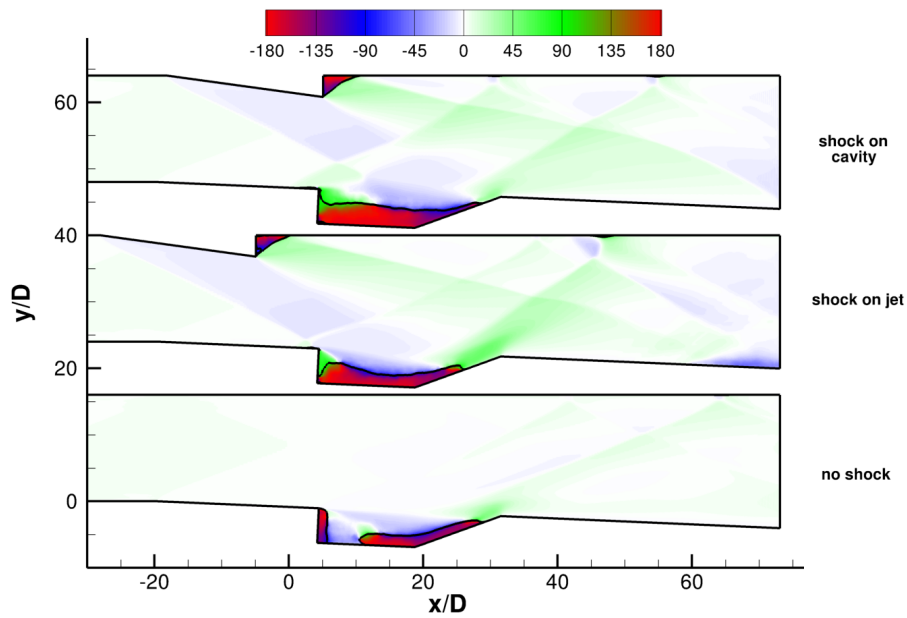
Figure 30: Flow Angle Relative to Bottom Wall from Time-Averaged LES/RANS
Simulation at z/D = -11.9

*White denotes flow from left to right, red denotes flow from right to left, green denotes upward flow, and
blue denotes downward flow. Black contour line denotes zero axial velocity.*
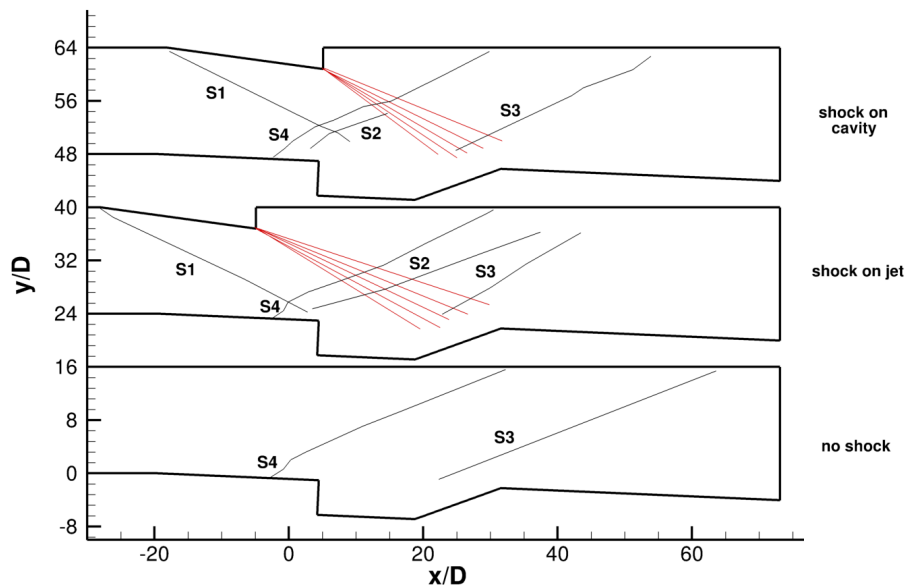
Figure 31: Wave Patterns Important to Cavity Mixing at Center Plane

Shocks in black, expansion fan in red.

indicating the zero velocity parallel to the bottom wall (i.e., the edge of the reversed flow zone). The center of rotation can be gleaned from the point around which the full spectrum of the contour levels is present, for instance at $x/D = 13$ and $y/D = -5$ in the No-Shock case in Figure 30. From these plots you can infer that the reversed flow zone in the No-Shock case extends from approximately $x/D = 10$ to the end of the cavity and the flow rotation is centered at about $x/D = 13$. In the Shock-On-Jet case the reversed flow zone is more upstream and the flow rotation is centered at about $x/D = 8$. For the Shock-On-Cavity case the reversed flow zone extends the length of the cavity and the flow rotation is centered at about $x/D = 13$.

With the knowledge of the off-center flow structures, the center plane flow structures with injection is easier to understand. Injection upstream of the cavity introduces a bow shock S4 as shown in Figures 31 – 32. In order to confirm that these shocks were correctly simulated, center plane temperature contours are compared with the ice crystal Mie scattering in Figures 33 – 35. The shape of the slower (and warmer) cavity flow is well-predicted for each case.

The flow angle contours for the center plane can be seen in Figure 36. They are much different than the flow angle contours in Figure 30. Specifically, the reversed flow section for the Shock-On-Cavity case is isolated to the cavity closeout ramp and the wake region of the jet. Also, the reversed flow region for the other two cases is larger on the centerplane than it was off-center. In order to better understand these phenomena, 3D iso-surfaces of the reversed flow boundary can be seen in Figures 37-39 as well as 3D

27
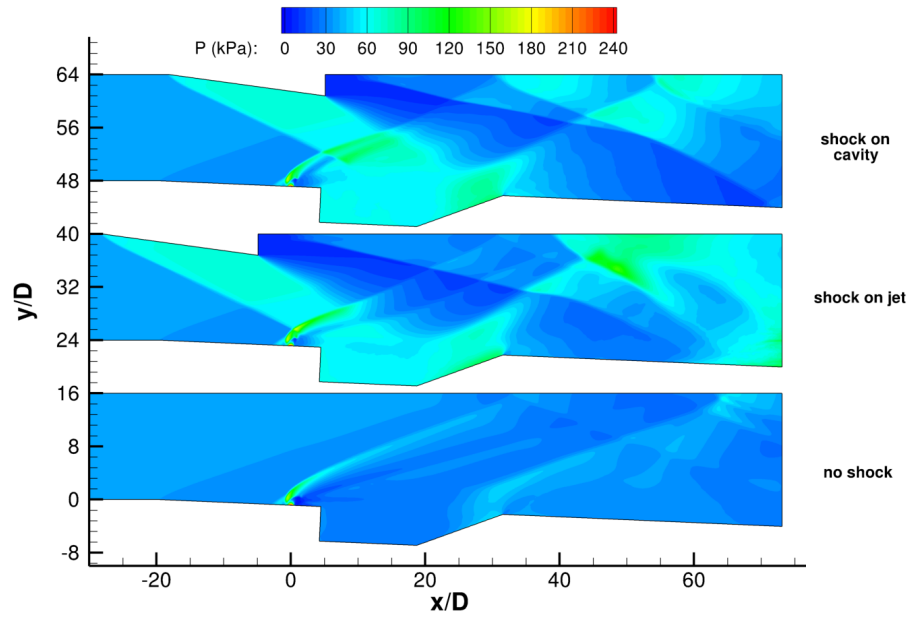
Figure 32: Contours of Time-Averaged Static Pressure at Center Plane

(a) Experimental Mie Scattering (b) LES/RANS Temperature

Figure 33: Time-Averaged Experimental Mie Scattering Ice Crystal and LES/RANS
contours of Temperature for No-Shock Case at Center Plane

(a) Experimental Mie Scattering   (b) LES/RANS temperature

Figure 34: Time-Averaged Experimental Mie Scattering Ice Crystal and LES/RANS
Contours of Temperature for Shock-On-Jet Case at Center Plane

(a) Experimental Mie scattering   (b) LES/RANS temperature
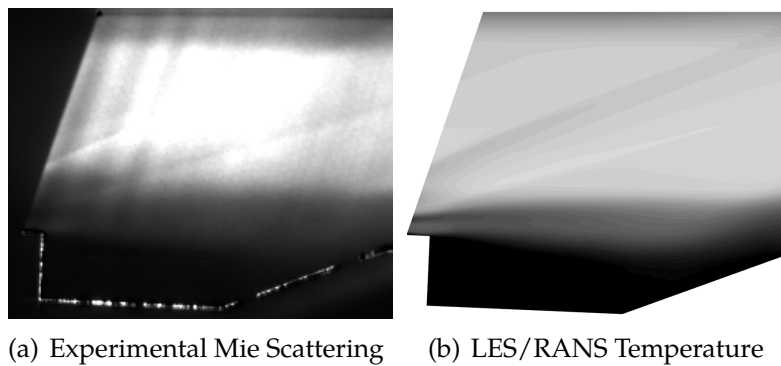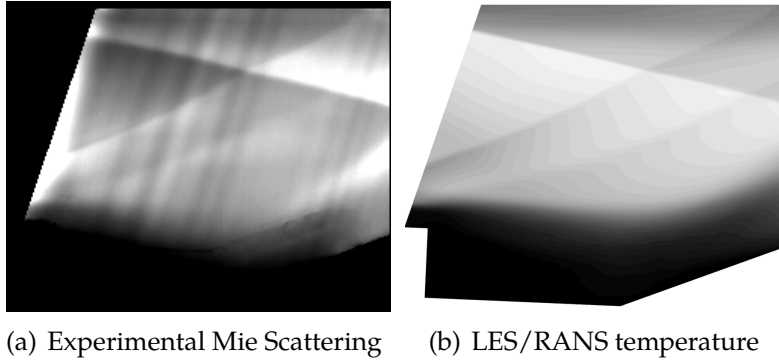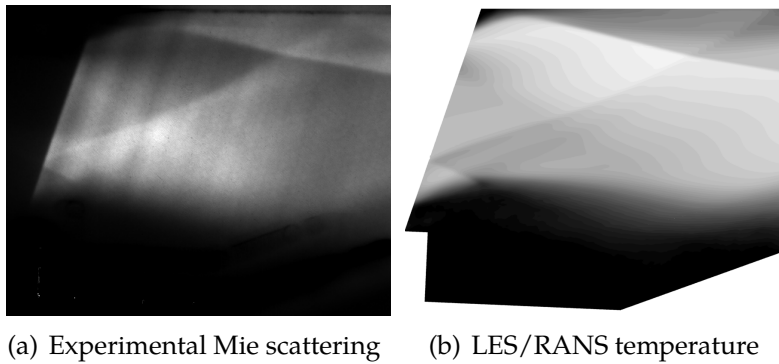
Figure 35: Time-averaged experimental Mie Scattering Ice Crystal and LES/RANS
Contours of Temperature for Shock-On-Cavity Case at Center Plane
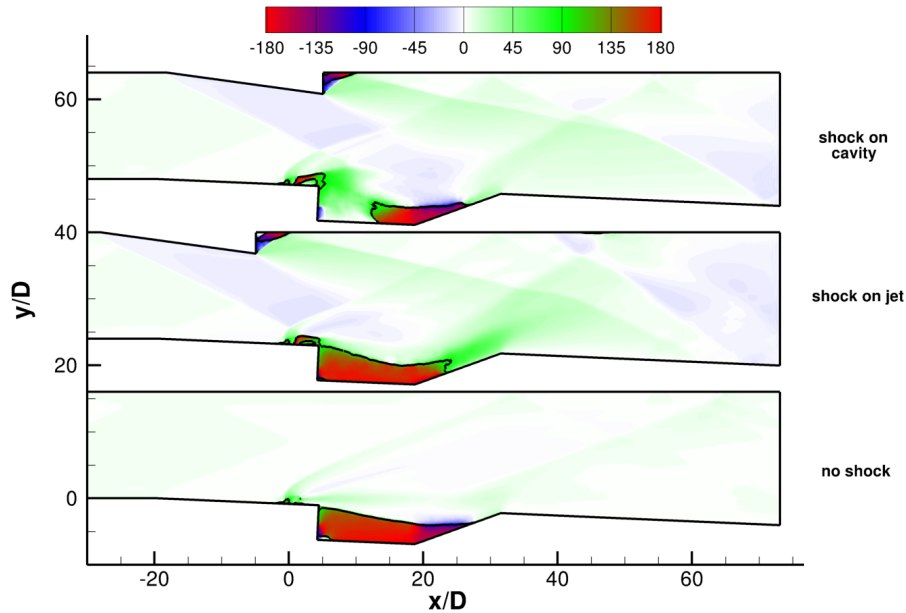
Figure 36: Flow Angle Relative to Bottom Wall from Time-Averaged LES/RANS
Simulation at $z/D = 0$

White denotes flow from left to right, red denotes flow from right to left, green denotes upward flow, and blue denotes downward flow. Black contour line denotes zero velocity parallel to divergent bottom wall.

injectant mass fraction iso-surfaces for each case.

The No-Shock iso-surface in Figure 37(a) shows a very small reversed flow region in the jet's wake. Also the plume itself carves out an un-reversed flow section in the middle of the cavity. The plume in Figure 37(b) shows no deflection toward the bottom wall and little lateral spreading of the injection in the cavity. The iso-surfaces for the Shock-On-Jet case in Figure 38(a) reveal two un-reversed flow regions on either side of the injectant plume at the upstream end of the cavity. In Figure 38(b), the plume is deflected toward the bottom wall due to the upstream oblique shock and the injectant on the bottom wall has moved further upstream than the No-Shock case. The Shock-On-Cavity case has an un-reversed flow section in the middle of the cavity just below the plumein Figure 39(a). As a result, the plume seen in Figure 39(b) does not move much upstream, but is instead pushed laterally away from the un-reversed flow section.

A comparison of the time-averaged Mach number on the centerplane is shown in Figure 40. This image more clearly shows the impact of the shock structure on the shear layer over the cavity.

The flow structures resulting from S1 and its position strongly impact the mixing downstream. Figure 41 shows the idealized wave diagram overlaid with injectant mass fraction. From this you can see that the unshocked case is the least mixed at the center plane. For the two shocked cases, they exhibit different patterns of mixing. The
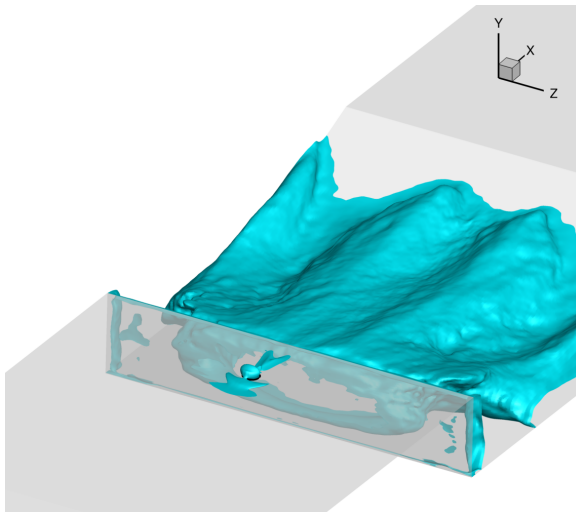
(a) Reversed flow
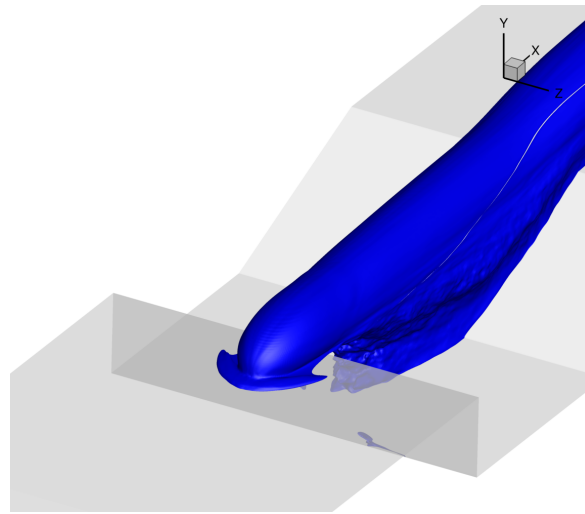
(b) $X_{inj} = 0.04$

Figure 37: 3D Iso-Surfaces for 'No-Shock' Case
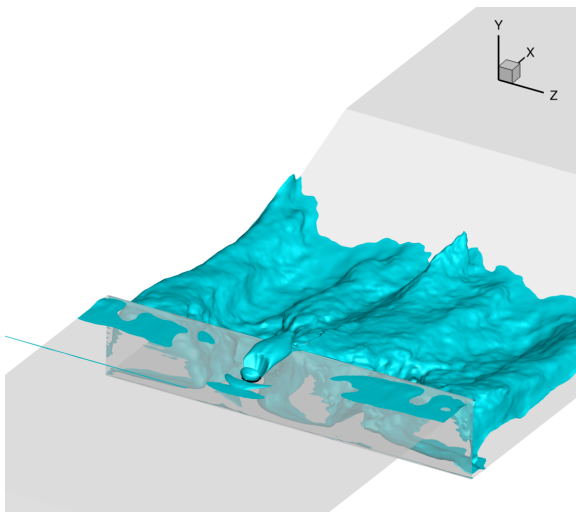
(a) Reversed Flow
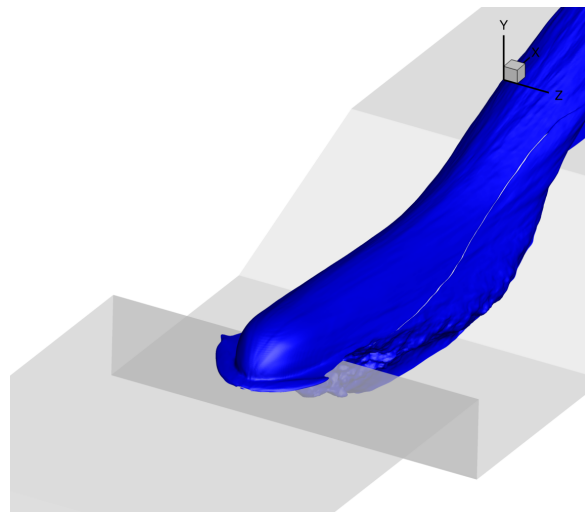
(b) $X_{inj} = 0.04$

Figure 38: 3D Iso-Surfaces for Shock-On-Jet Case

31

(a) Reversed Flow   (b) $X_{inj} = 0.04$
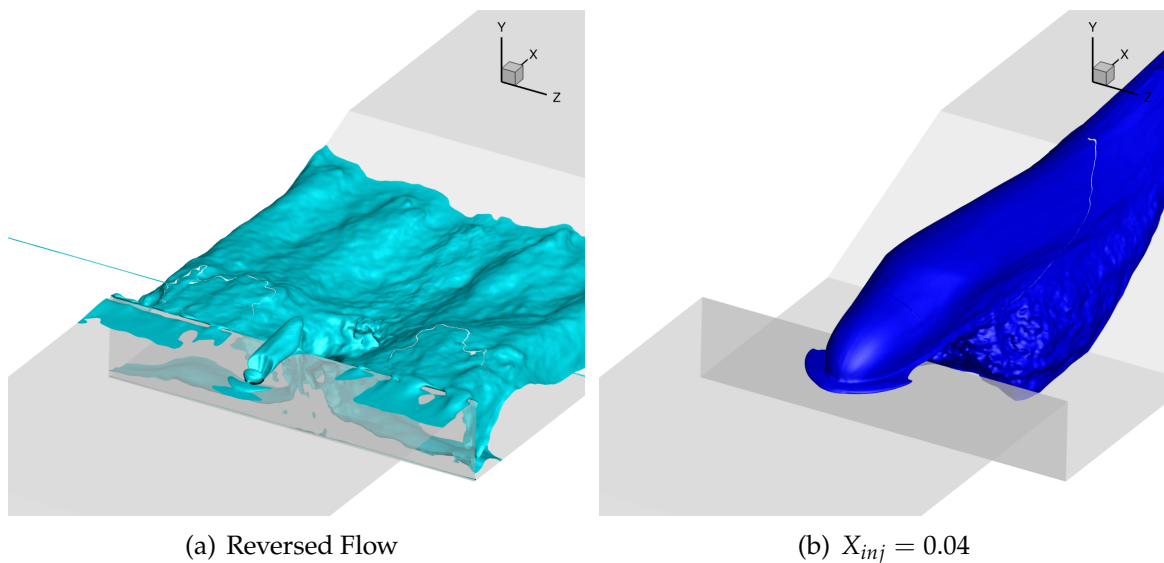
Figure 39: 3D Iso-Surfaces for Shock-On-Cavity Case
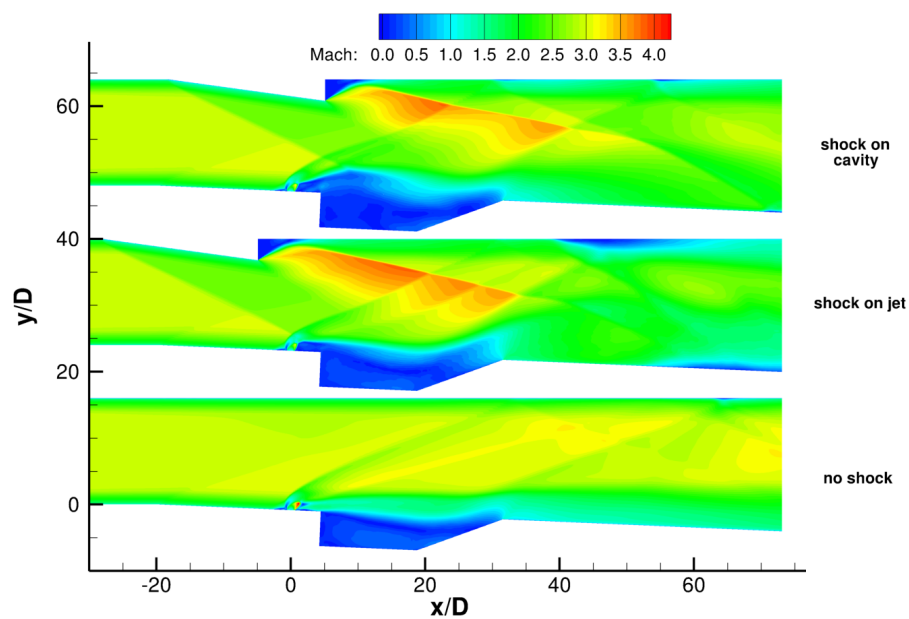
Figure 40: Center Plane Contours of Time-Averaged Mach Number

32
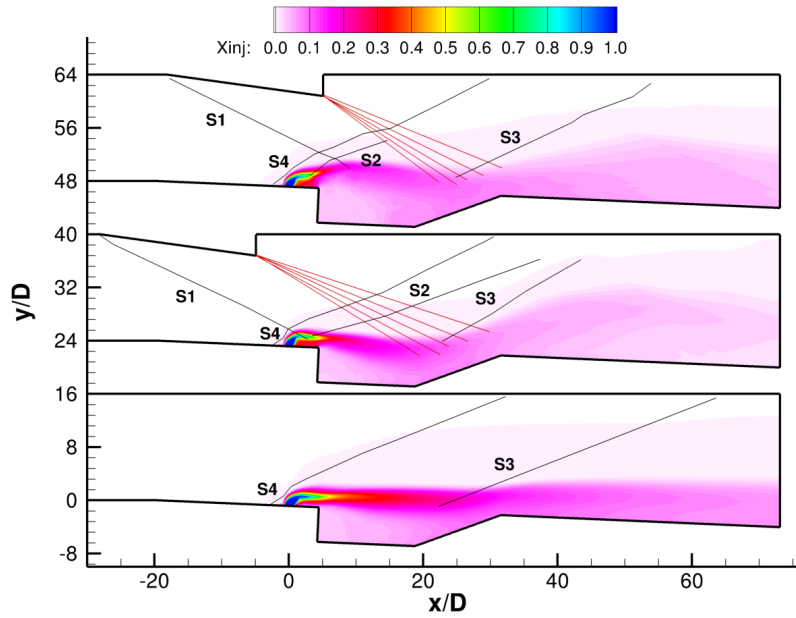
Figure 41: Time-Averaged Injectant Mass Fraction Contours with Idealized Wave Structures

(a) Experimental NO-PLIF

(b) LES/RANS Injectant Mass Fraction

Figure 42: Time-Averaged Experimental NO-PLIF Imagery and LES/RANS Contours of Injectant Mass Fraction for No-Shock Case at Center Plane

(a) Experimental NO-PLIF

(b) LES/RANS Injectant Mass Fraction

Figure 43: Time-Averaged Experimental NO-PLIF Imagery and LES/RANS Contours of Injectant Mass Fraction for Shock-On-Jet Case at Center Plane

(a) Experimental NO-PLIF

(b) LES/RANS Injectant Mass Fraction

Figure 44: Time-Averaged Experimental NO-PLIF Imagery and LES/RANS Contours of Injectant Mass Fraction for Shock-On-Cavity Case at Center Plane
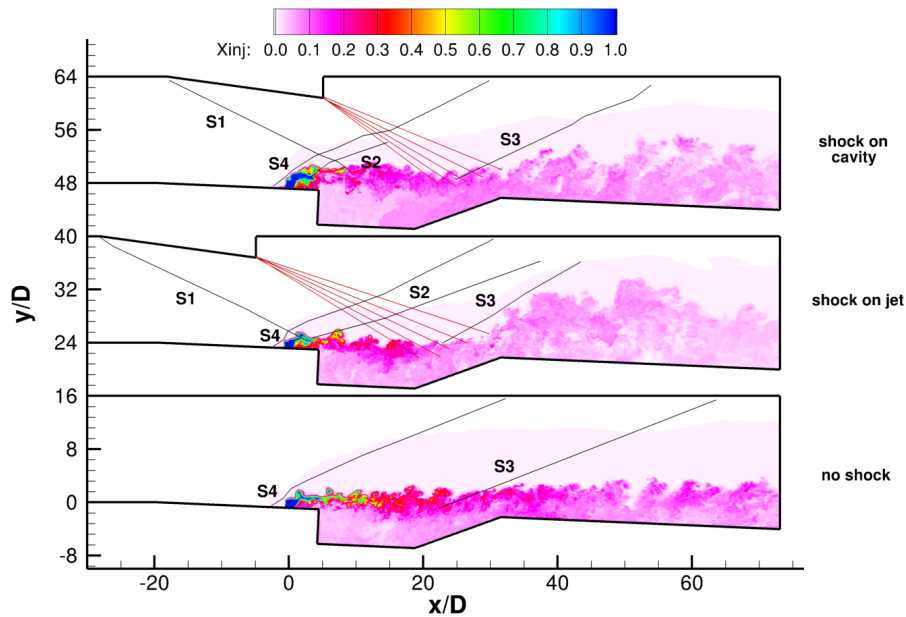
Figure 45: Center Plane Contours of Instantaneous Injectant Mass Fraction

Shock-On-Jet case shows an injection plume that initially turns down toward the bottom wall but then sharply turns away from the bottom wall after crossing through the expansion fan and S3. The Shock-On-Cavity case sees the plume rise from the bottom wall initially because of the large cavity recirculation zone caused by the impinging shock. Downstream of S1 the plume starts to move toward the bottom wall and then turns away from the bottom wall as it proceeds through the expansion fan and S3, but not as much as the Shock-On-Jet case. The behavior of these plumes in the LES/RANS simulation was also observed in the NO-PLIF experimental imagery seen in Figures 42–44.

Figure 45 shows the same idealized wave structures as Figure 41 on top of an instantaneous injectant mass fraction distribution as predicted by the LES/RANS simulations. In addition to mean information, NO-PLIF experimental also provides information on the instaneous plume shape in a given plane. Figures 46–48 show center plane NO-PLIF images compared with instantaneous injectant mass fraction for the LES/RANS simulations. As with all the NO-PLIF comparisons, they are qualitative in nature as the brightness and contrast is adjusted for each image. The plume structures in the No-Shock case are the least diffuse in the simulation as well as the experimental images. Also the Shock-On-Cavity simulation shows the most diffuse plume with the least defined plume structures.

Slices at constant axial locations in Figures 49–51 show the differences in mixing off-center. Note that these images only show about half the computational domain width. The most basic observation is that the shocked cases mix much more fully than the unshocked case. Also, the Shock-On-Cavity case shows more lateral spreading in the
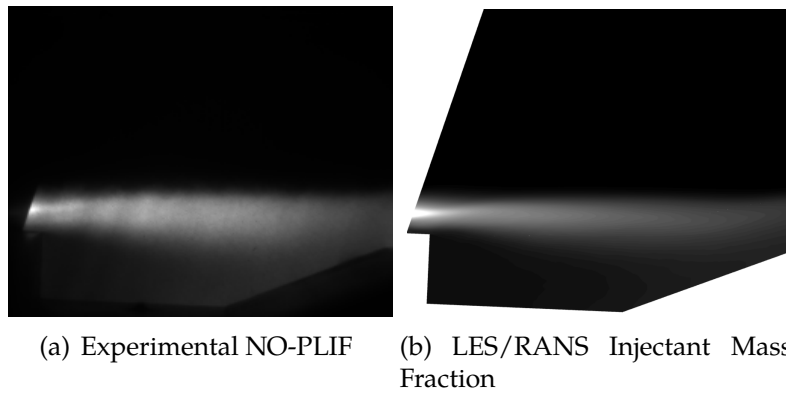
(a) Experimental NO-PLIF

(b) LES/RANS Injectant Mass Fraction

Figure 46: Snapshots of Experimental NO-PLIF Imagery and LES/RANS Contours of Injectant Mass Fraction for No-Shock Case at Center Plane

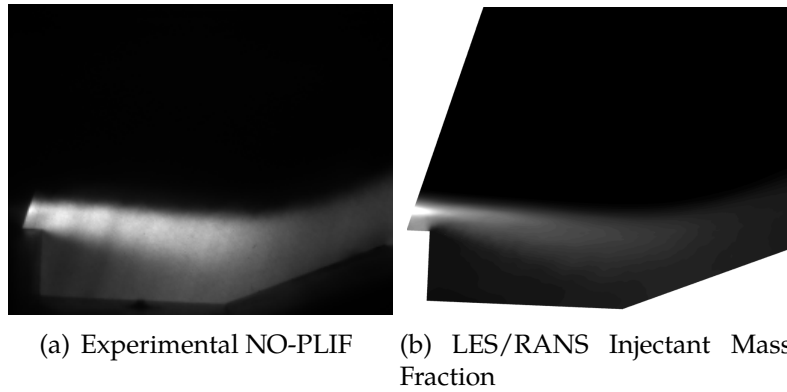
(a) Experimental NO-PLIF

(b) LES/RANS Injectant Mass Fraction

Figure 47: Snapshots of Experimental NO-PLIF Imagery and LES/RANS Contours of Injectant Mass Fraction for Shock-On-Jet Case at Center Plane

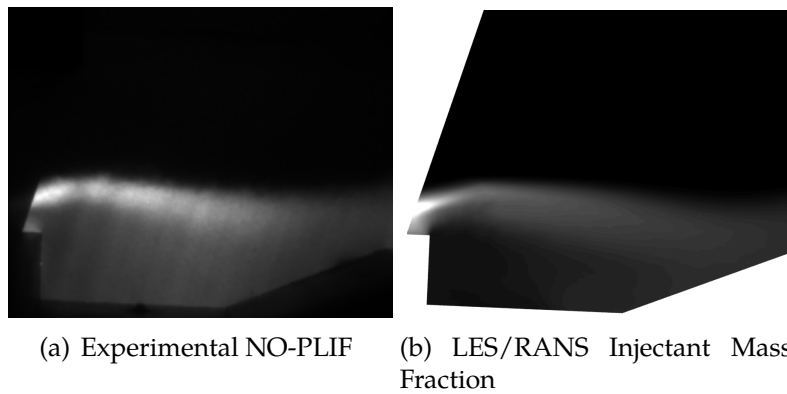(a) Experimental NO-PLIF

(b) LES/RANS Injectant Mass Fraction

Figure 48: Snapshots of Experimental NO-PLIF Imagery and LES/RANS Contours of Injectant Mass Fraction for Shock-On-Cavity Case at Center Plane
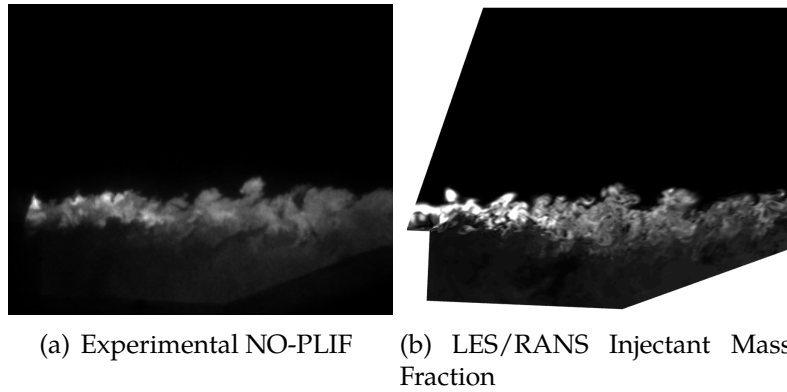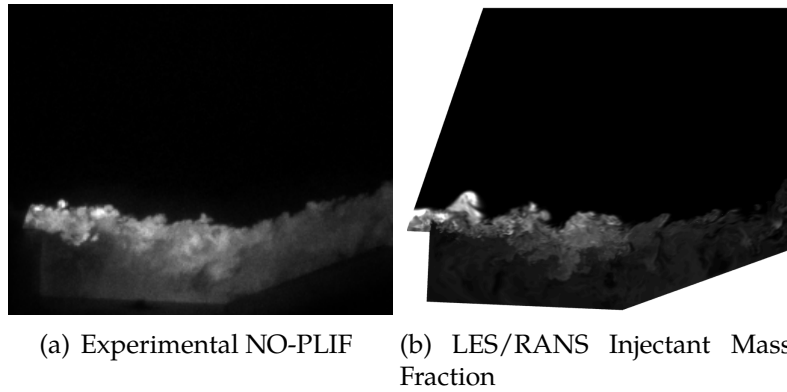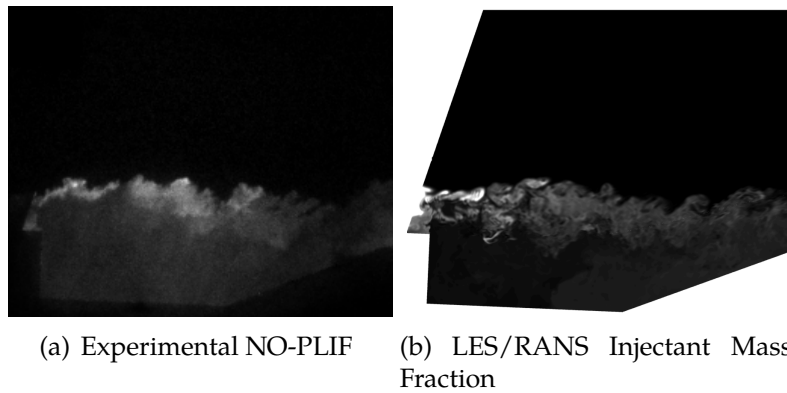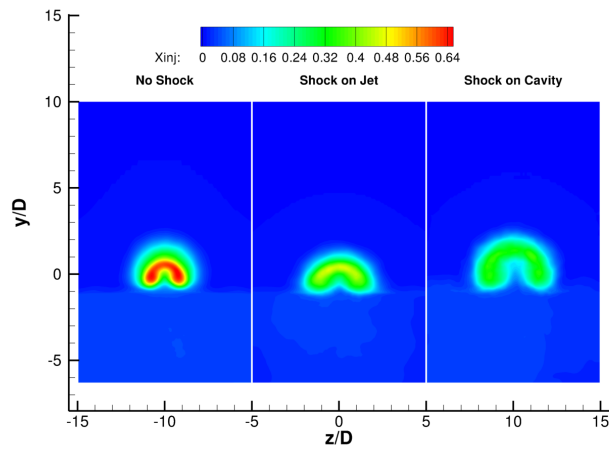
Figure 49: Time-Averaged LES/RANS Contours of Injectant Mass Fraction for q=1, x/D = 5
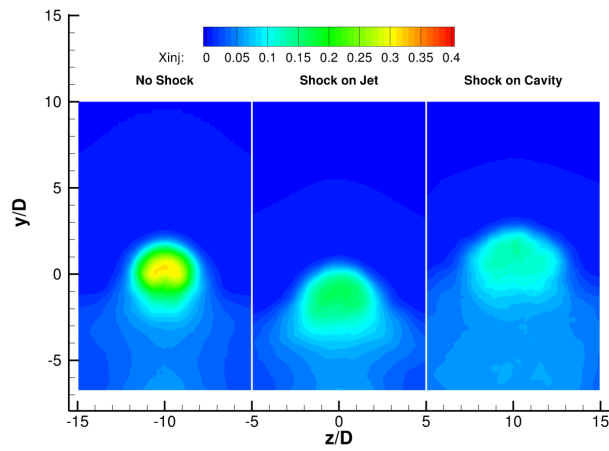
Figure 50: Time-Averaged LES/RANS Contours of Injectant Mass Fraction for q=1, x/D = 15
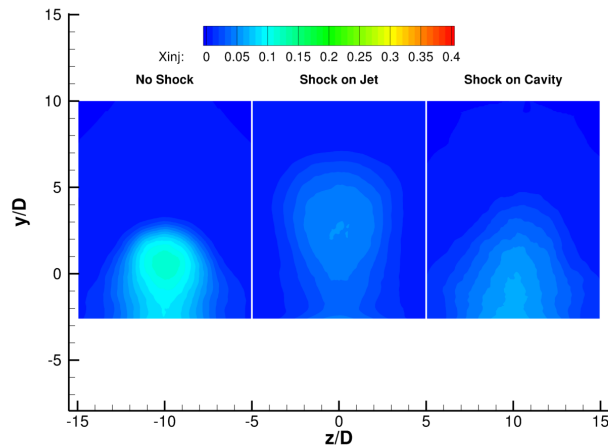
Figure 51: Time-Averaged LES/RANS Contours of Injectant Mass Fraction for q=1, x/D = 40

cavity than the other two cases. Also, at the first station in Figure 49, it is notable that the lower bound of the counter-rotating vortices line up along the shear layer for all three cases, but the shape and mixing of these vortices varies widely between the three. The top of the counter-rotating vortex pair for the Shock-On-Cavity case is lifted substantially and there is a distinct spatial separation between the vortex pair at the center. The vertical penetration is increased due to the the outward displacement of the shear layer seen in Figure 40.

4.3.2   Reacting Flow Cases

The outline of the solution domain is shown in Figure 52 and represents a half-width of the RC19 flowpath, with the symmetry plane shaded in blue. The domain includes the Mach 3.0 facility nozzle. The overall length of flowpath is 45 inches, and has a 2 by 6 inches cross-section at the end of the nozzle, but with the symmetry assumption only 3 inches of the width are simulated . All walls were modeled using a turbulent wall function with a maximum y^+ equal to 80, and were assumed to be adiabatic.

On the centerline is the primary (jet) injector which is upstream of the cavity and one of the cavity injectors. There are a total of eleven cavity injectors in the full-width, spaced in half inch increments. Five full injectors and one half injector are included in the simulation. The fuel injectors used the measured mass flowrate and fuel plenum total temperature as a boundary condition. The outflow was set to a supersonic outflow boundary condition. The bottom wall grid surface topology of the cavity is shown in Figure 53. Figure 54 shows the exploded view of some of the cavity injectors which have a diameter of 0.078 inches. The centerline of each injector is 0.1 inches above the bottom wall of the cavity and the ramp angle is $67.5°$ from the normal.

The 15×15 notation on the figure represents the number of computational nodes that
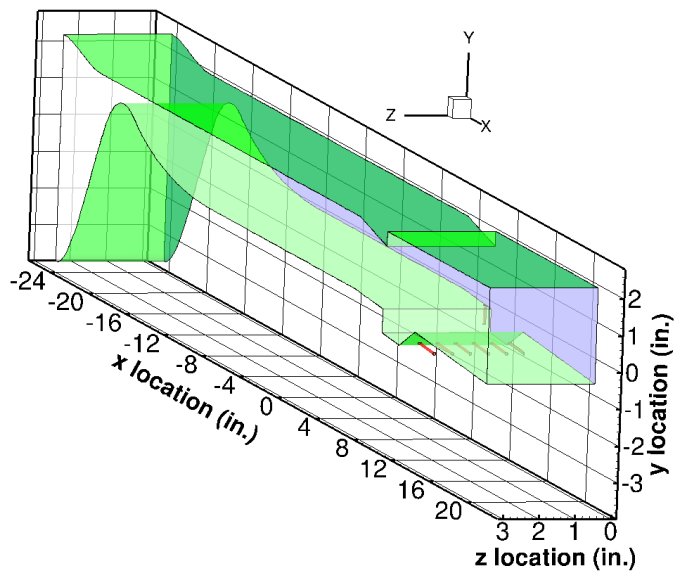
Figure 52: Outline of Cavity Flowpath Half-Geometry
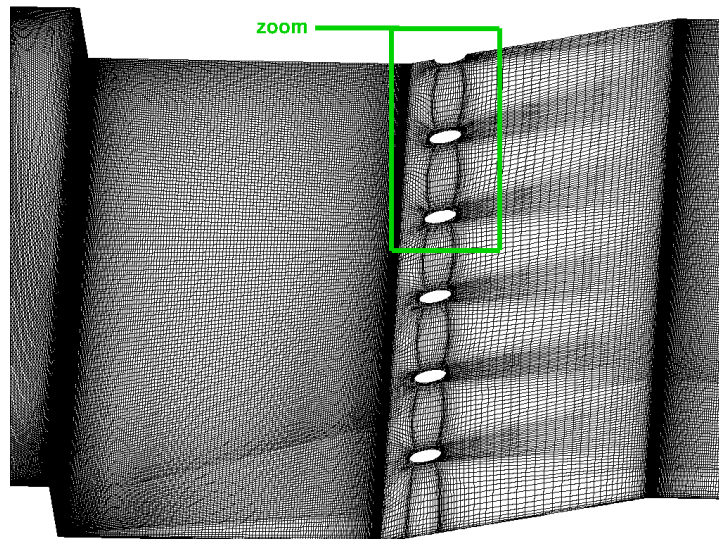
Figure 53: Cavity Bottom-Wall Grid Topology Showing Cavity Injectors (CFD++ RANS simulations)
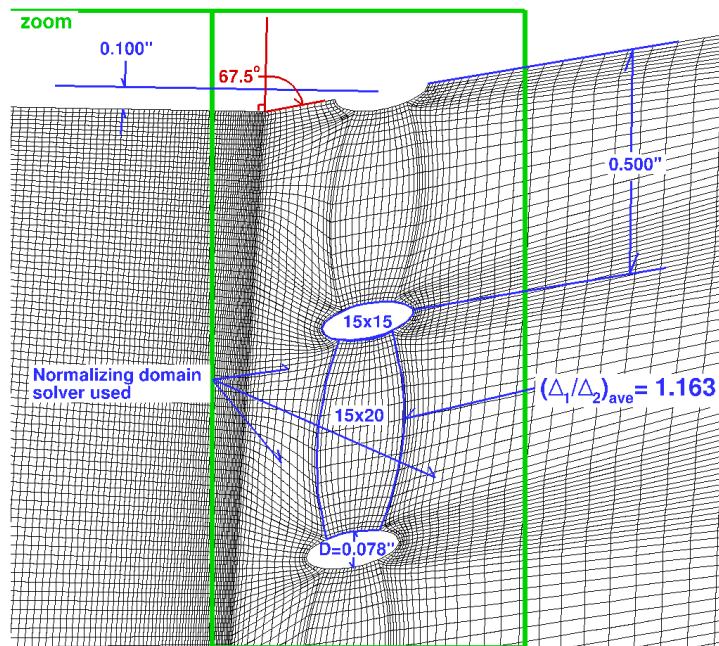
Figure 54: Cavity Bottom-Wall Grid Topology Showing Cavity Injectors (CFD++ RANS simulations) – detail
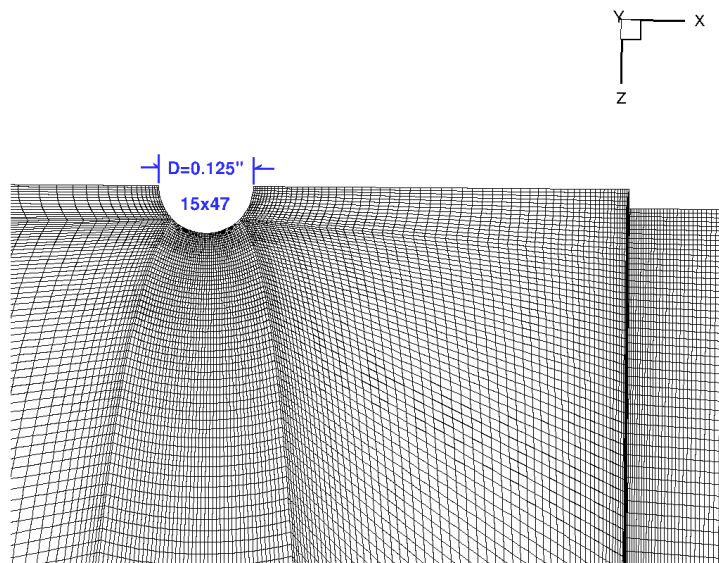
Figure 55: Cavity Bottom Wall Grid Topology of Upstream Primary Injector
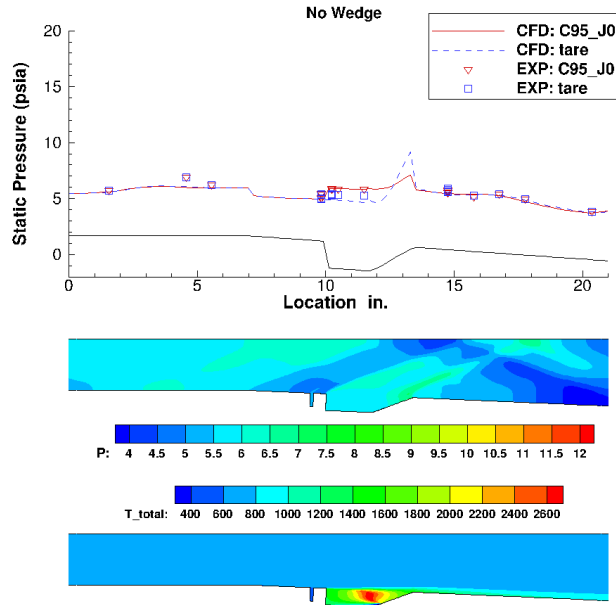
Figure 56: Center-Line Bottom Wall Pressure and Center Plane Pressure and Total Temperature Contours for No-Shock Case with Cavity Only Fueling

span the cross-section of each cavity injector exit. There are 15×20 nodes between each injector and the average stretching ratio for the spanwise connector between each injector is 1.163, which represents the greatest average stretching in the computational domain. An elliptic smoother was used to minimize skewness. The primary injector exit is shown in Figure 55. The injector diameter is 0.125 inch with a 15×47 nodal cross-section.

Figure 56 shows wall pressure and CFD centerline contours of static pressure and total temperature. Shown in the figure is the tare case and reacting case for the No-Shock flowpath with cavity only fueling (95 slpm). Notice there is no shock train development upstream of the cavity for the case with reactions and the pressure rise in the cavity is minimal. Contours of Mach number (not shown) were consistent in revealing that the core flow remained supersonic throughout. This means the isolator flow upstream of the cavity was largely undisturbed by the chemical reactions. Neither the experiment nor CFD saw a change in isolator wall pressure due to the addition of fuel. Two of the three isolator wall pressures compare favorably between the experiment and the CFD with the exception of the middle pressure tap (at approximately 4.5 inches). This experimental value exceeded the CFD by 13 percent but the other two only exceeded by 2 percent. The higher middle pressure was consistent throughout the test, and is likely due to a weakly reflected wave from the nozzle-isolator- interface. The cavity pressures (specifically, at approximately 11.5 inches) show a small increase in pressure between tare and reacting. The experiment showed approximately 12 percent increase and the CFD showed approximately 20 percent. The two are consistent and compare reasonably well, but the CFD underpredicts the tare pressure in the cavity by approximately 10 percent from the experiment.

Figure 57: CFD OH Mass Fraction Contours and Experimental OH-PLIF Imagery for No-Shock Case with Cavity Only Fueling

Figure 58: Centerline Bottom Wall Pressure and Center Plane Pressure and Total Temperature Contours for No-Shock Case with Cavity and Primary Fueling

Streamwise slices of OH mass fraction in Figure 57 indicate that significant burning occurs on the cavity ramp. OH-PLIF suggests the location of burning is similar to that of the CFD. The CFD and experiment have the same general distribution of OH. Also, there is negligible spanwise variation in OH for both the CFD and experiment which suggests spanwise uniformity.

Figure 58 shows the pressure distribution for the same No-Shock case, but with both cavity and primary injector fueling. The cavity fueling rate was reduced by 50% to 47 slpm and the primary fuel injection rate was 350 slpm. The wall pressure remained mostly unchanged by the addition of primary fuel as compared to cavity only fueling shown previously in Figure 56. The CFD and experiment show a small increase in pressure toward the exit of the domain. The pressure discontinuity upstream of the cavity from the CFD data is due to the primary injection plume and is not the result of combustion.

Figure 59 shows the OH mass fraction slices for the CFD (left) and experiment (right). Along the centerline, both the CFD and experiment show minimal amounts of OH in the cavity. For this case most of the diatomic oxygen was burned, but diatomic hydrogen was present. The mass fraction of carbon monoxide was twice as much as the case with cavity only fuel. The additional fuel from the primary injector increased the fuel fraction along the centerline which burned most of the oxygen and elevated temperatures, however overall burn quality was poor. The first two off-centerline slices of OH show gradually increasing levels of OH from the experiment, the CFD did not capture this gradual increase and showed significantly higher levels of OH in the first off-centerline slice. The last two off-centerline slices show distinct levels of OH along the shear layer
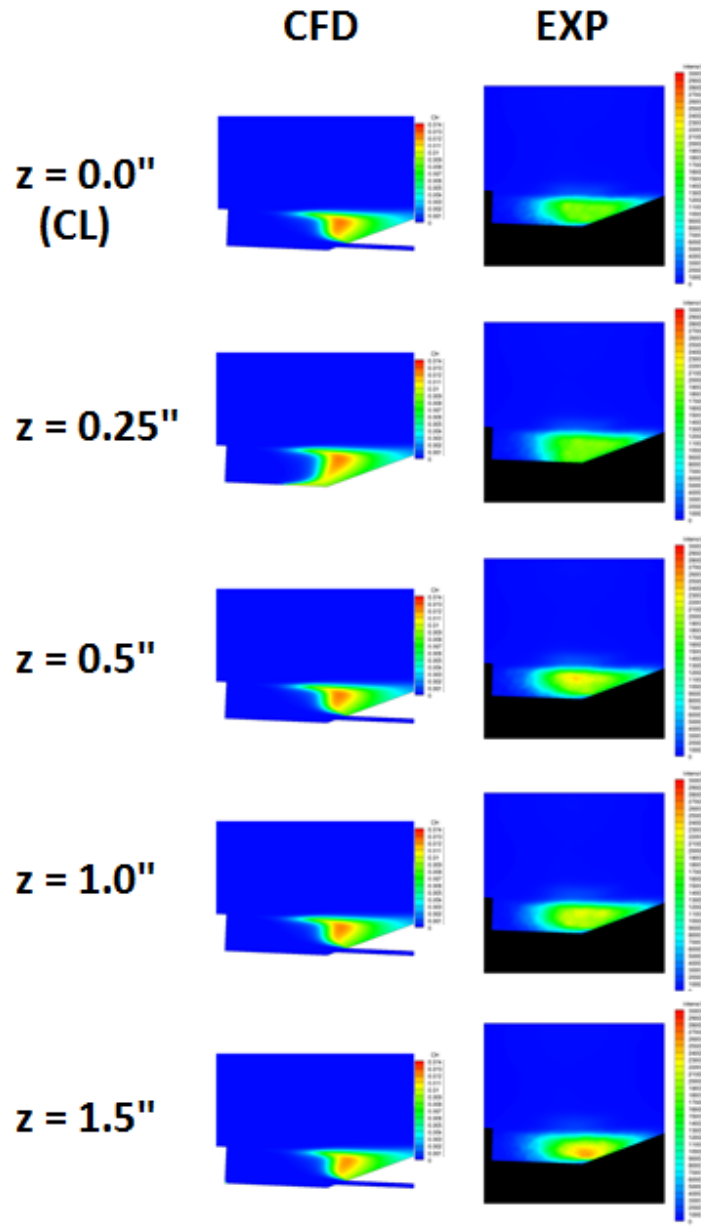
43

Figure 59: CFD OH Mass Fraction Contours and Experimental OH-PLIF Imagery for No-Shock Case with Cavity and Primary Fueling
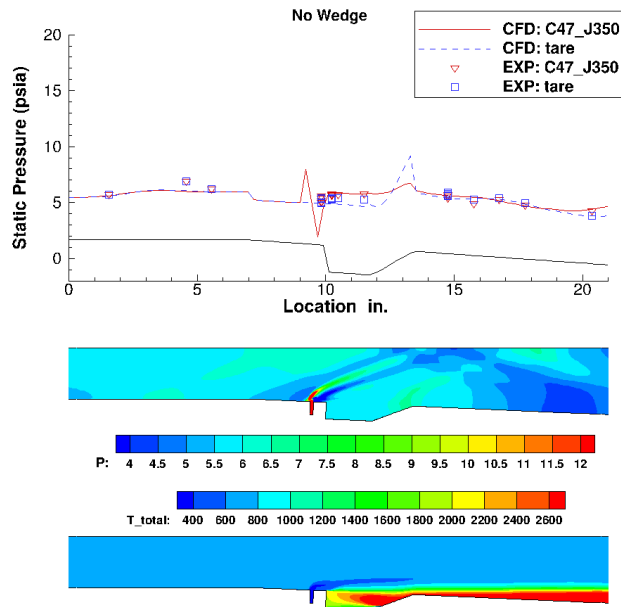
Figure 60: Centerline Bottom Wall Pressure and Center Plane Pressure and Total Temperature Contours for Shock-On-Cavity Case with Cavity Only Fueling

over the cavity from both the CFD and experiment.

The case with the 8° wedge in its most downstream position (Shock-On-Cavity) creates a pressure rise throughout the cavity as shown in Figure 60. With combustion the pressures in the cavity increases by 15% and the core flow remains supersonic. The CFD and experiment compare well and both show a pressure rise near the exit of the domain. It appears little burning occurs along the centerline of the cavity as shown by the low temperatures in the total temperature contour.

The first two OH slices in Figure 61 show no OH production in the CFD and minimal intensities from the experiment. The experiment shows a gradual increase in OH from one off-centerline slice to another. The CFD shows a gradual increase as well. Most of the OH occurs in the upstream portion of the cavity which is shown in both the CFD and experimental observations.

Figure 62 shows the case with the 8° wedge in its same position but with primary fuel injection. With combustion the pressure rise across the cavity is 25% greater than tare. Once again there is no thermal choking. Both the CFD and experiment show a significant pressure rise near the exit of the domain downstream of the cavity. The total temperature contour clearly shows that there is flow turning downstream of the cavity; with combustion this contributes to the downstream pressure rise.

Figure 63 shows OH slices from the CFD and experiment. A stark contrast with primary fueling can be observed on the centerline as compared to the previous case that had cavity only fuel. Both the CFD and experiment show significant levels of OH in the cavity along with elevated levels protruding into the core flow. The shape and location of
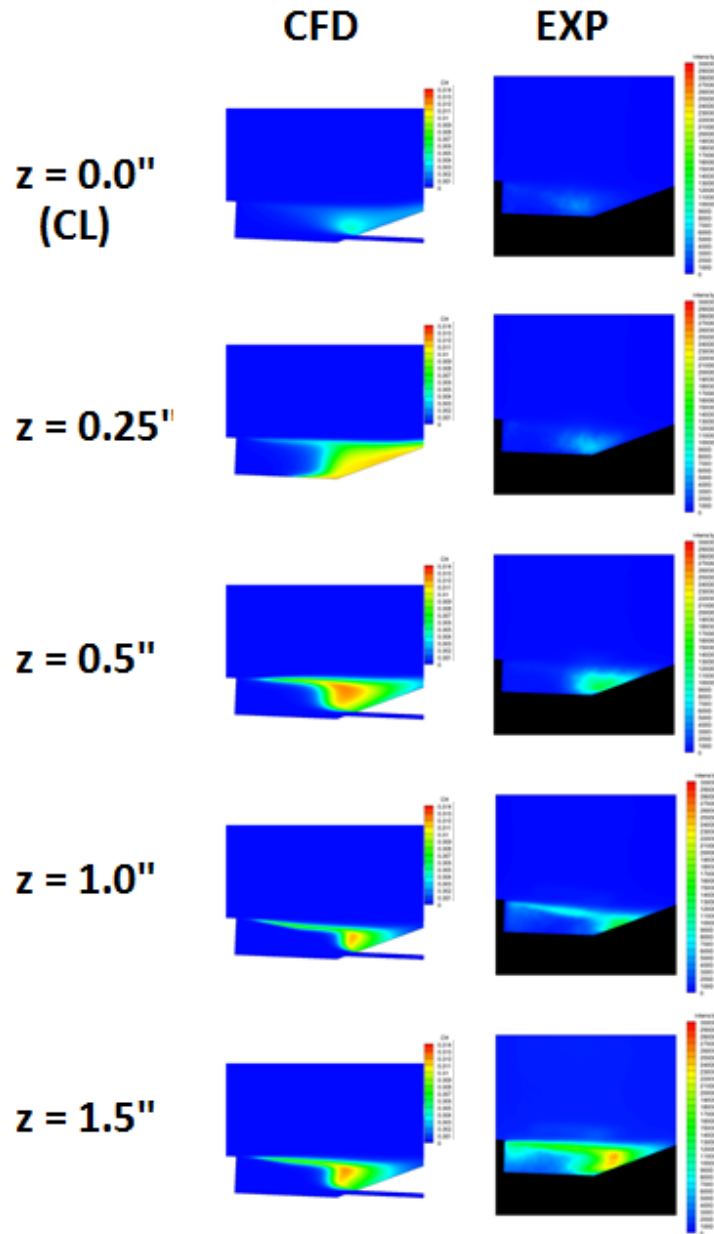
45

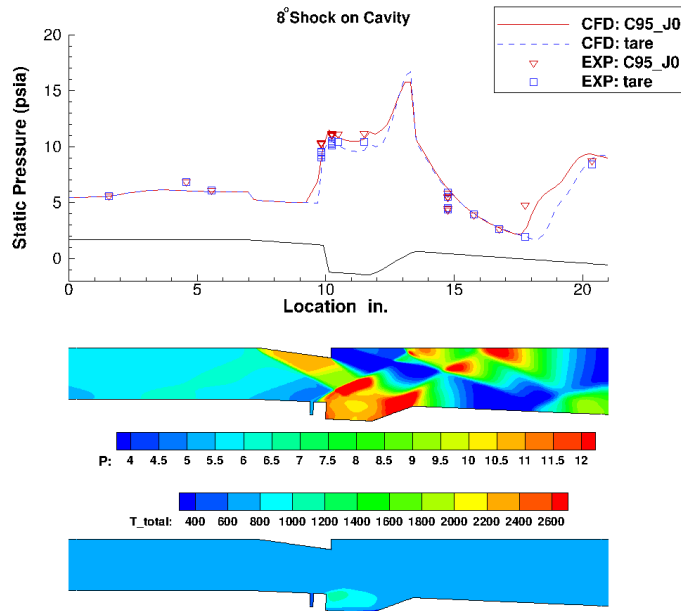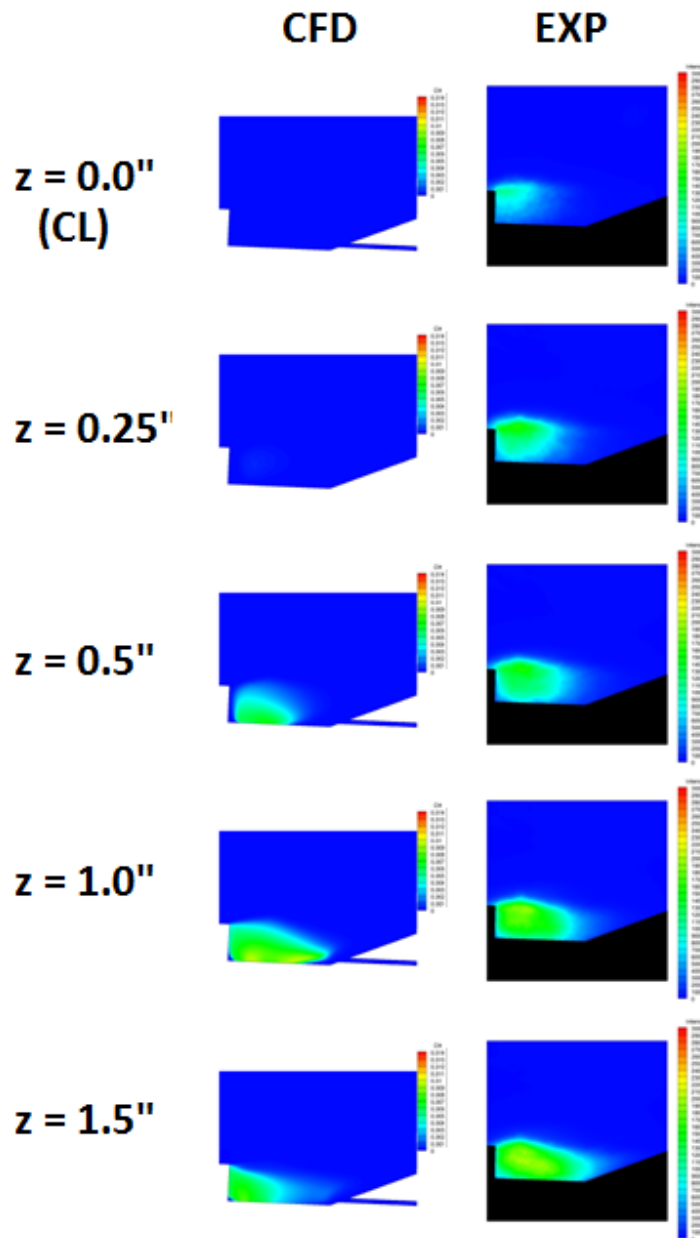Figure 61: CFD OH Mass Fraction Contours and Experimental OH-PLIF Imagery for Shock-On-Cavity Case with Cavity Only Fueling

Figure 62: Centerline Bottom Wall Pressure and Center Plane Pressure and Total Temperature Contours for Shock-On-Cavity Case with Cavity and Primary Fueling

OH agree very well at all spanwise locations.

The next case is the Shock-Upstream case which never lit during the experiment, thus only tare is shown in Figure 64. The pressure distribution between the experiment and CFD agree very well. Notice the strong shock that hits the upstream injector and the expansion that runs over the cavity. The next section of the analysis reviews mixing results related to this case to better understand why this case never lit.

Figure 65 shows bottom wall equivalence ratio contours for three separate mixing cases. All three cases have cavity only fueling at 95 slpm. As shown before, the No-Shock and Shock-On-Cavity cases were capable of lighting and sustaining combustion. The black cross shown in each image represents the spark plug location. The contour limits range from $0 < \Phi < 1.0$. An equivalence ratio (Φ) = 1.0 represents an ideal fuel-air mixture quantity which is the most ideal mixture for ignition from a forced ignition source. The No-Shock case shows that the spark plug is located in a region with $\Phi > 1.0$ which represents a fuel rich region. The Shock-On-Cavity case shows the spark plug exists at the edge of a fuel-rich and fuel-lean region as does the Shock-Upstream position.

Figure 66 shows a contour of Φ for the No-Shock case and the black solid line represents the axial location of the spark plug and the black dotted line represents an outline of the top of the cavity. 1D data properties were extracted along the black solid line and are shown in the 1D plot. The grey region in the 1D plot represents the flammability region for forced ignition. This region is approximate and is based on empirical flammability limits of ethylene data taken at standard atmospheric conditions. The equivalence ratio is ≈ 1.4 near the cavity floor and ≈ 1.5 along the wall normal. This means the fuel-air mixture was well within the flammability limits despite the low cavity pressure of 5 psia

Figure 63: CFD OH Mass Fraction Contours and Experimental OH-PLIF Imagery for Shock-On-Cavity Case with Cavity and Primary Fueling

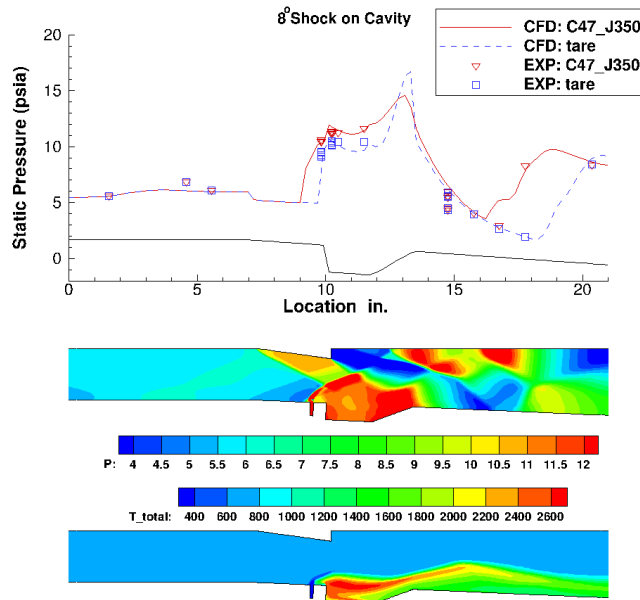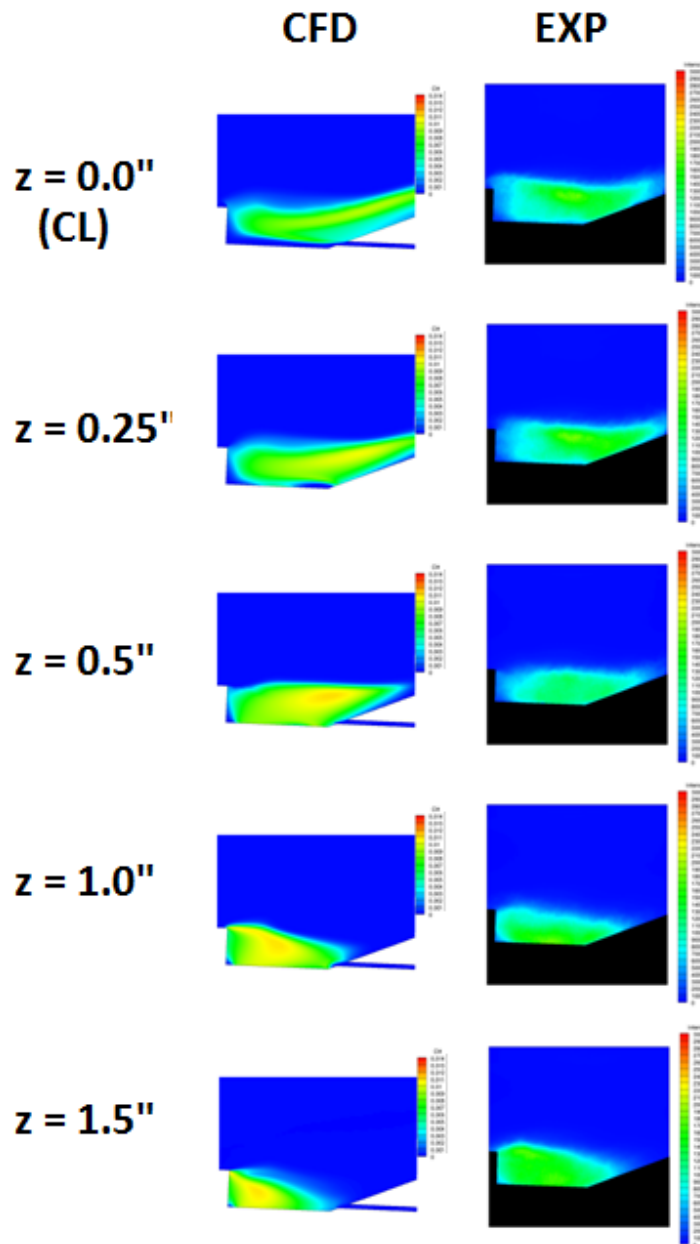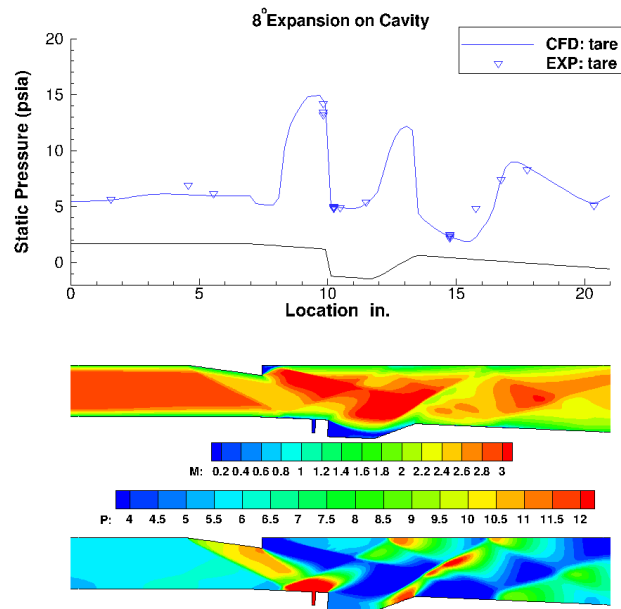Figure 64: Centerline Bottom Wall Pressure and Center Plane Pressure and Total
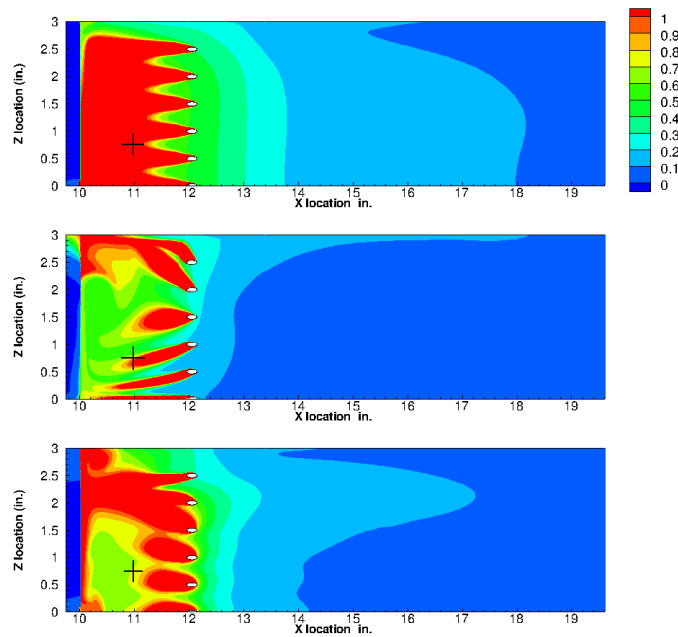Temperature Contours for Shock-Upstream with No Fueling

Figure 65: Equivalence Ratio Distribution on Bottom Wall for Mixing Only Cases

(from top to bottom – No-Shock case, Shock-On-Cavity case and Shock-Upstream case).

Figure 66: Center Plane Equivalence Ratio at x=11 in. Showing Flammability Limits, and Center Plane Equivalence Ratio Contours for No-Shock Case

which is shown by the green line.

Figure 67 shows the Shock-On-Cavity case, with the wedge in its downstream position. It shows a much different Φ distribution in the cavity. The 1D shows a lean fuel-air mixture near the wall (Φ ≈ 0.8), but the mixture is within the lower flammability limit (LFL). Away from the wall the mixture leans out and falls outside of the flammability limits. The pressure at the wall is nearly double the No-Shock case because of the shock impinging on the cavity, the pressure is approximately 9.5 psia.

Figure 68 shows the Shock-Upstream case, with the wedge in its upstream position. This case has a very similar profile as the Shock-On-Cavity case. Near the wall and at the location of the spark plug the fuel-air mixture is lean (Φ ≈ 0.7), but is within the prescribed flammability limits. In contrast, the pressure near the wall is lower at 5 psia which is similar to the wall cavity pressure of the No-Shock case. Thus it appears there should have been enough fuel available to ignite the cavity given the upstream wedge position.

The following three images in Figure 69 show streamtraces coming out of the centerline cavity injector. Notice in the image on the left the fuel is entering and exiting the cavity in the same streamwise plane and the recirculation zone in the cavity is large and follows the whole perimeter of the cavity. The Shock-On-Cavity case shows a similar result as the No-Shock, except one streamtrace shows some fuel being diverted off centerline and exiting the cavity near the side wall. The Shock-Upstream position is in direct contrast to the other two. It shows the fuel entering the cavity on centerline and all the fuel exits the cavity off centerline. The recirculation zone is suppressed, narrow, and does not follow the entire perimeter of the cavity.

50
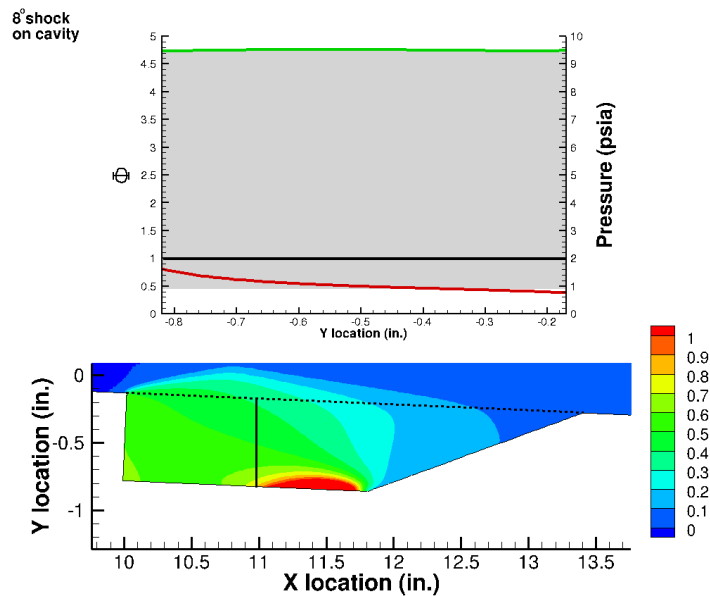
Figure 67: Center Plane Equivalence Ratio at x=11 in. Showing Flammability Limits, and Center Plane Equivalence Ratio Contours for Shock-On-Cavity Case
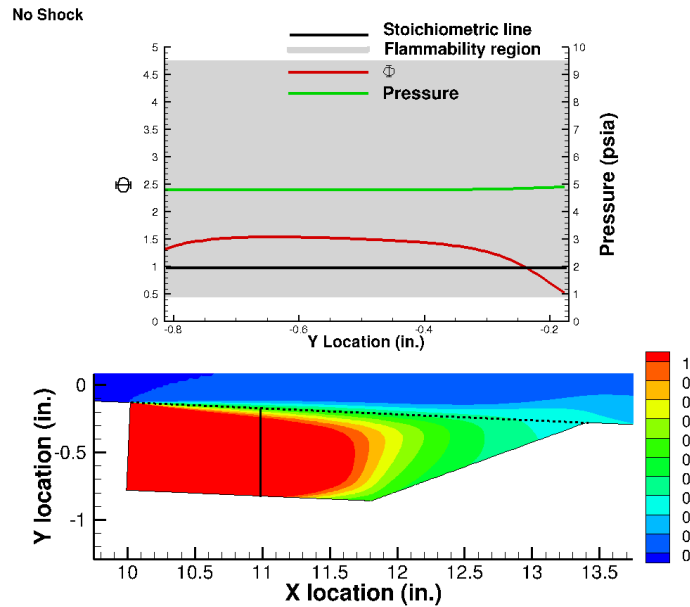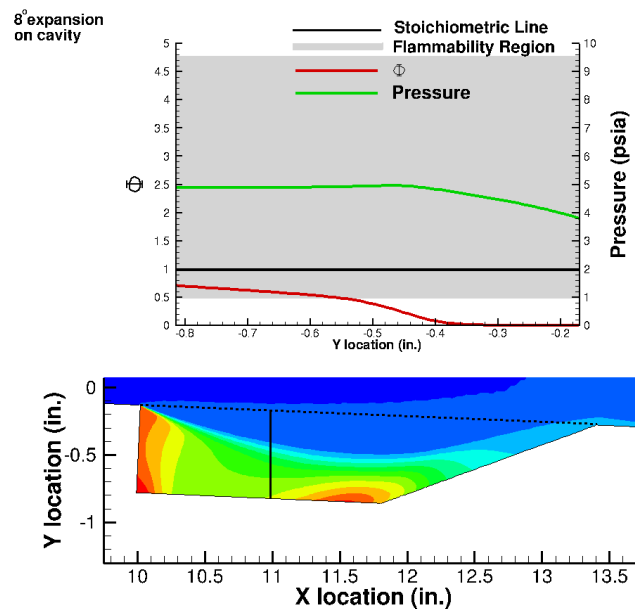

Figure 68: Center Plane Equivalence Ratio at x=11 in. Showing Flammability Limits, and Center Plane Equivalence Ratio Contours for Shock-Upstream Case

51

(a) No-Shock   (b) Shock-On-Cavity   (c) Shock-Upstream
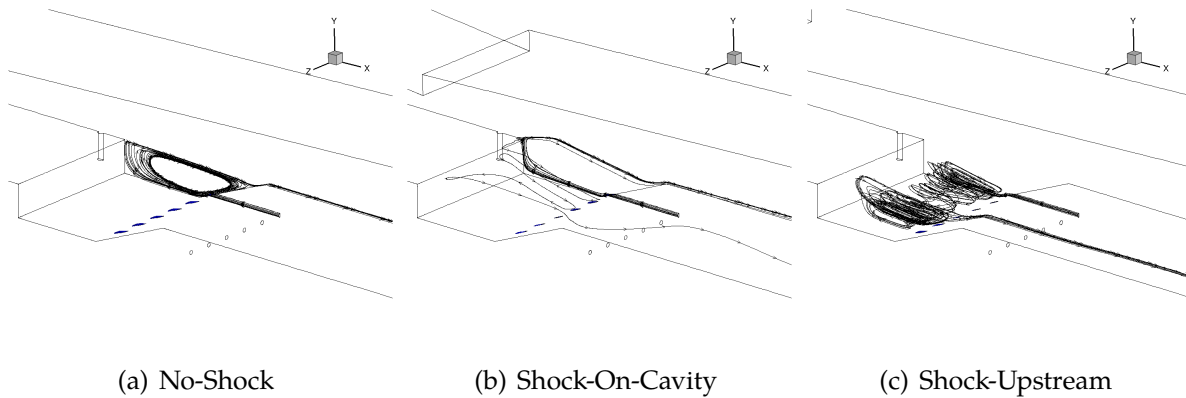
Figure 69: Cavity Fuel Streamtraces

Fine grid RANS simulations of the Shock-On-Jet case with cavity only fueling were performed using the REACT-MB solver in preparation for an LES/RANS simulation of that case. For these simulations, the same grid as was used for the nonreacting flow, Shock-On-Jet case was used. The Mawid six species, three reaction ethylene combustion model [28] was used with inert nitrogen as the seventh species. For the results shown, the Mawid model was altered by decreasing the activation temperatures by 50 percent. Further investigation was not performed to assess the need for this alteration.

Figures 70 – 72 show a comparison between the REACT-MB results and the CFD++ results. As can be seen, there is more water present in the CFD++ contours than with REACT-MB. The hybrid LES/RANS results showed evidence of earlier burning. These results reflect instantaneous values early in the calculation, and converged mean values were not obtained during the course of this effort.

(a) CFD++ RANS   (b) REACT-MB RANS   (c) LES/RANS
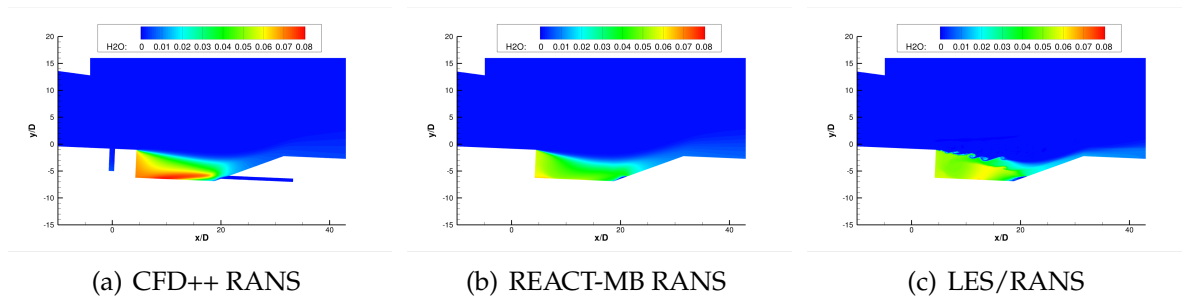
Figure 70: Contours of Water Mass Fraction at Center Plane for Shock-On-Jet Case with Cavity Fueling

52

(a) CFD++ RANS   (b) REACT-MB RANS   (c) LES/RANS
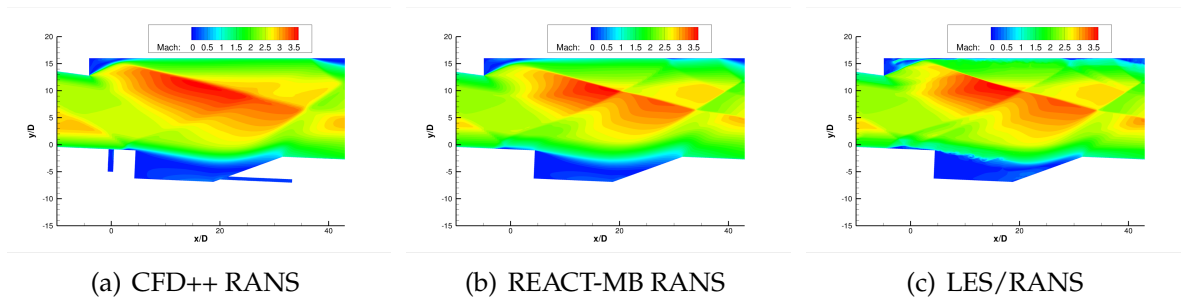
Figure 71: Contours of Mach Number at Center Plane for Shock-On-Jet Case with Cavity Fueling

(a) CFD++ RANS   (b) REACT-MB RANS   (c) LES/RANS
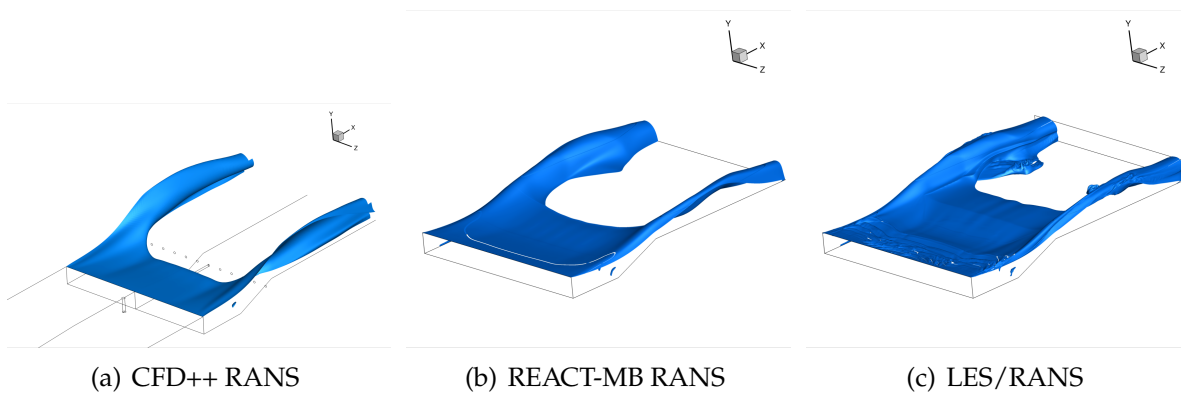
Figure 72: 3D Iso-Surface of 1% Water Mass Fraction

5 Conclusions

RANS and hybrid LES/RANS computation models have been applied to various problems related to flow distortion in scramjet flows. For the cases where supporting experimental data is available, good agreement has been shown. In addition to the insights gained on the validity of the computational models, we have gained insight into the effects of flow distortion.

Hybrid LES/RANS simulations of sonic injection of ethylene into a Mach 2 crossflow have been compared with new experimental NO-PLIF and high-frequency shadowgraph imagery of air injection with inflow distortion. The impact of the tested 5-degree shock generator on mixing has been shown was shown to be minimal. The LES/RANS model was very capable of predicting the mixing and the impact of the 5-degree shock generator on the mixing of the injectant. A 7-degree shock generator configuration was also simulated, though that has not been tested experimentally yet. This configuration shows even more mixing than the 5-degree generator due to further slowing of the flow. Unfortunately this shock causes a large separation in the wall boundary layer as well as a significant drop in total pressure.

RANS and hybrid LES/RANS were used to simulate shock distortion for cavity-assisted mixing and combustion. The shock impingement in the cavity region was shown to have a significant effect on both the non-reacting flow, in which the shear layer over the cavity was either lifted or depressed dependent on the shock position relative to the cavity. Both RANS and LES/RANS models accurately modeled this displacement of the shear layer. This effect carried over into the reacting studies, where the ability to ignite the cavity was fundamentally changed by the location of the shock. RANS simulations showed good agreement with the cases that did ignite experimentally. Also, a simulation of the nonigniting case shed light on possible causes of the ignition issue. The combusting hybrid LES/RANS simulations were not completed, but showed potential for high-quality predictions. Further pursuit of hybrid LES/RANS simulation of combusting ethylene is recommended.

6 References

[1] Gruber, M. R., Hagenmaier, M. A., and Mathur, T., "Simulating Inlet Distortion Effects in a Direct-Connect Scramjet Combustor," AIAA Paper 2006–4680, Sacramento, CA, July 2006.

[2] Lin, K.-C., Ryan, M., Carter, C., Gruber, M., and Raffoul, C., "Raman Scattering Measurements of Gaseous Ethylene Jets in Mach 2 Supersonic Crossflow," *Journal of Propulsion and Power*, Vol. 26, No. 3, May–June 2010, pp. 503–513.

[3] Gruber, M. R., Nejad, A. S., Chen, T. H., and Dutton, J. C., "Transverse Injection from Circular and Elliptic Nozzles into a Supersonic Crossflow," *Journal of Propulsion and Power*, Vol. 16, No. 3, 2000, pp. 449–457.

[4] Mathur, T., Streby, G., Gruber, M., Jackson, K., Donbar, J., Donaldson, W., Jackson, T., Smith, C., and Billig, F., "Supersonic Combustion Experiments with a Cavity-Based Fuel Injector," AIAA Paper 99–2102, Los Angeles, CA, June 1999.

[5] Gruber, M. R., Baurle, R. A., Mathur, T., and Hsu, K.-Y., "Fundamental Studies of Cavity-Based Flameholder Concepts for Supersonic Combustors," *Journal of Propulsion and Power*, Vol. 17, No. 1, 2001, pp. 146–153.

[6] Spalart, P. R., Jou, W.-H., Strelets, M., and Allmaras, S. R., "Comments on the Feasibility of LES for Wings and of a Hybrid RANS/LES Approach," *Advances in DNS/LES*, edited by C. Liu and Z. Liu, Greyden Press, Dayton, OH, 1998, pp. 137–147.

[7] Spalart, P. R., Deck, S., Shur, M. L., Squires, K. D., Strelets, M., and Travin, A., "A New Version of Detached-Eddy Simulation, Resistant to Ambiguous Grid Densities," *Theoretical and Computational Fluid Dynamics*, Vol. 20, No. 3, May 2006, pp. 181–195.

[8] Hassan, E., Aono, H., Boles, J., Davis, D., and Shyy, W., "Multi-Scale Turbulence Model Simulation of Supersonic Crossflow," AIAA Paper 2010–111, Orlando, FL, January 2011.

[9] Palekar, A., Truman, C. R., and Vorobieff, P., "Prediction of Transverse Injection of a Sonic Jet in Supersonic Crossflow," AIAA paper 2005-5366, Toronto, Ontario, June 2005.

[10] Boles, J. A., Edwards, J. R., and Baurle, R. A., "Large-Eddy/Reynolds-Averaged Navier-Stokes Simulations of Sonic Injection into Mach 2 Crossflow," *AIAA Journal*, Vol. 48, No. 7, July 2010, pp. 1444–1456.

[11] Maddalena, L., Campioli, T. L., and Schetz, J. A., "Experimental and Computational Investigation of Light-Gas Injectors in Mach 4.0 Crossflow," *Journal of Propulsion and Power*, Vol. 22, No. 5, 2006, pp. 1027–1038.

[12] Davis, D. L., *Numerical Analysis of Two and Three Dimensional Recessed Flame Holders for Scramjet Applications*, Ph.D. thesis, Air Force Institute of Technology Air University, September 1996.

[13] Kim, K. M., Baek, S. W., and Han, C. Y., "Numerical Study on Supersonic Combustion with Cavity-Based Fuel Injection," *International Journal of Heat and Mass Transfer*, Vol. 47, 2004, pp. 271–286.

[14] http://legacy.mae.ncsu.edu/research/cfd_lab/index.html.

[15] Boles, J. A., Choi, J.-I., Edwards, J. R., and Baurle, R. A., "Multi-Wall Recycling / Rescaling Method for Inflow Turbulence Generation," AIAA Paper 2010–1099, Orlando, FL, January 2010.

[16] Edwards, J. R., "A Low-Diffusion Flux-Splitting Scheme for Navier-Stokes Calculations," *Computers & Fluids*, Vol. 26, No. 6, 1997, pp. 635–659.

[17] Colella, P. and Woodward, P. R., "The Piecewise Parabolic Method (PPM) for Gas-Dynamical Simulations," *Journal of Computational Physics*, Vol. 54, 1984, pp. 174–201.

[18] http://metacomptech.com.

[19] Liu, J., Tam, C.-J., Lu, T., and Law, C. K., "Simulations of Cavity-Stabilized Flames in Supersonic Flows Using Reduced Chemical Kinetic Mechanisms," AIAA Paper 2006–4862, Sacramento, CA, July 2006.

[20] Sullins, G. and McLafferty, G., Tech. rep.

[21] Schetz, J. A., Maddalena, L., and Burger, S. K., "Molecular Weight and Shock-Wave Effects on Transverse Injection in Supersonic Flow," *Journal of Propulsion and Power*, Vol. 26, No. 5, September 2010, pp. 1102–1113.

[22] Campioli, T. L., Maddalena, L., and Schetz, J. A., "Studies of Shock Wave/Transverse Injection Interaction on Supersonic Mixing Processes," AIAA Paper 2006–8135, Canberra, Australia, July 2010.

[23] Gruber, M. R. and Nejad, A. S., "New Supersonic Combustion Research Facility," *Journal of Propulsion and Power*, Vol. 11, No. 5, 1995, pp. 1080–1083.

[24] Boles, J., Milligan, R., Hagenmaier, M., Eklund, D., and Edwards, J., "Hybrid Large-Eddy Simulation / Reynolds-Averaged Navier-Stokes Simulation of Sonic Injection into Mach 2 Crossflow," AIAA Paper 2011–769, Orlando, FL, January 2011.

[25] Fric, T. F., "Skewed Shear Layer Mixing Within a Duct," AIAA Paper 95-0869, Reno, NV, January 1995.

[26] Etheridge, S., Carter, C. D., and Lee, J., "Characterization of Supersonic Flow Interaction with Shockwaves Using Laser-based Diagnostics," 2012, to be presented at 2012 Joint Propulsion Conference.

[27] Rasmussen, C. C., Driscoll, J. F., Hsu, K.-Y., Donbar, J. M., Gruber, M. R., and Carter, C. D., "Stability limits of cavity-stabilized flames in supersonic flow," *Proceedings of the Combustion Institute*, Vol. 30, 2005, pp. 2825–2833.

[28] Baurle, R. A. and Eklund, D. R., "Analysis of Dual-Mode Hydrocarbon Scramjet Operation at Mach 4 – 6.5," AIAA Paper 2001–3299, Salt Lake City, UT, July 2001.

LIST OF ACRONYMS, ABBREVIATIONS, AND SYMBOLS

Acronyms

AFRL   Air Force Research Laboratory

AOA   angle of attack

BSL   baseline

CFD   computational fluid dynamics

DNS   direct numerical simulation

LDFSS   Low-Diffusion Flux-Splitting Scheme

LES   large eddy simulation

LFL   lower flammability limit

NO-PLIF   nitrous oxide-planar laser-induced fluorescence

OH-PLIF   OH planar laser-induced fluorescence

PPM   Piecewise Parabolic Method

RANS   Reynolds-averaged Navier-Stokes

SBLI   shockwave-boundary layer interaction

slpm   standard liters per minute

Roman Symbols

c time-averaged mixture fraction

$\bar{c}$ planar- and time-averaged mixture fraction

D   jet diameter

k turbulent kinetic energy

M mixedness parameter

Pr_t turbulent Prandtl number

q   momentum flux ratio

Sc_t turbulent Schmidt number

u_τ friction velocity

y^+ dimensionless, sublayer-scaled, distance, $u_\tau y/\nu$, at first grid point away from surface

Y_f fuel mass fraction

Y_t fuel mass fraction threshold

Greek Symbols

α blanking variable for plume edge calculation

ϵ turbulence dissipation

ν kinematic molecular viscosity

ρ_f species density of fuel

Φ equivalence ratio